UNIVERSITY OF OSLO

Department of Physics

Investigation of electronic and structural properties of silicon solar cell contacts

Thesis submitted for degree of Master of Science in Materials, Energy and Nanotechnology

Domas Birenis

1st June, 2012

Preface

This thesis is a final project of Master degree program in ‘Materials, energy and nanotechnology’ at University of Oslo. It was performed at Fermio laboratory in Forskningsparken, Oslo in collaboration with Institute of Energy Technology (IFE), department of Solar Energy at Kjeller.

It was a great pleasure and experience to work with people from both institutions. My greatest gratitude goes to my supervisors Anette Eleonora Gunnæs and Erik Stensrud Marstein for help in planning, discussion, performing experiments and writing my thesis. I also wish to thank Hallvard Angelskår, Frode Kløw and Nicoleta Popovici for high-quality training sessions, helpful ideas and thoughts. Special thanks to Dan Phuong Nguyen, Thomas Qureishy for fruitful talks and advices on TEM and other topics.

I finally would like to thank my parents for invaluable support and trials to understand the physics of solar cells and electron microscopy; it really helped to understand these things myself. Last but not least thanks to my girlfriend for motivation and encouragement.

Domas Birenis

Oslo 2012

Abstract

Screen-printing technique is used since 1970's, but the understanding of screen printed contacts is quite poor. Several different models of contact formation exist. Two mechanisms of current transport from bulk semiconductor to bulk metal are proposed but not experimentally proved. Metal/semiconductor (Ag/Si) interface is the most important part of screen-printed contact and reduction of series resistance between the bulk Ag and the Si wafer has a large potential for solar cell performance improvement. Composition of the silver paste together with firing parameters is the most important players in formation of well conducting metal/semiconductor interface.

Commercially available silver pastes which are used for front contacts consist of silver powder, lead-glass frit powder and an organic vehicle. A crucial condition which determines the quality of the contact is firing temperature. During firing, the glass frit plays a critical role as it forms a glassy layer between the Si wafer and the bulk Ag, works as a medium for diffusion of Ag and Pb particles and is responsible for etching the SiN layer. In order to enhance solar cells' performance it is important to explain how contact formation depends on firing temperature and to improve understanding of electron transport between the Si wafer and the silver contact.

In this work, an Ag-Pb based paste was used and peak firing temperature (PFT) was varied in order to get optimally fired (best performance), under fired and over fired (lower performance) cells. Electronic properties of the cells were investigated using a solar simulator and a series resistance mapping technique. Transmission Electron Microscopy (TEM) imaging, Selected Area Diffraction (SAD) and Energy Dispersive Spectroscopy (EDS) techniques were used to study the structure and chemistry of the metal/semiconductor interfaces.

The results show that in under fired cells the PFT was too low to etch away the SiN layer which works as an insulating layer and impedes current collection. In optimally fired cells the PFT was high enough to partly etch away the SiN layer. In areas with no SiN, glassy layer with many Ag and Pb precipitates is in direct contact with the Si wafer. Distances between precipitates are <3 nm and current is efficiently collected through tunneling. In over fired cells SiN is completely etched away. Larger Ag crystallites are found on the Si interface. In the vicinity of these crystallites, the number of Ag and Pb precipitates in the glassy phase decreases and particles increase in size. Distances between precipitates become too large for electrons to tunnel and series resistance increases.

Contents

1. Introduction

Worldwide energy demand has been continuously increasing and is not expected to stop on a nearest time perspective. This phenomenon introduces two major problems of global warming and the need for alternative energy sources.

Last International Energy Outlook shows that world energy consumption could increase by 53 percent from $5{,}3 \cdot 10^{20}$ Joules in 2008 to $8{,}1 \cdot 10^{20}$ Joules in 2035 (Fig. 1.1). In the near term, the effects of the global recession of 2008-2009 reduced the growth of world energy consumption, but as nations recover from the decline, world energy demand will rapidly increase as a result of robust economic growth and expanding populations in the world's developing countries [1.1].

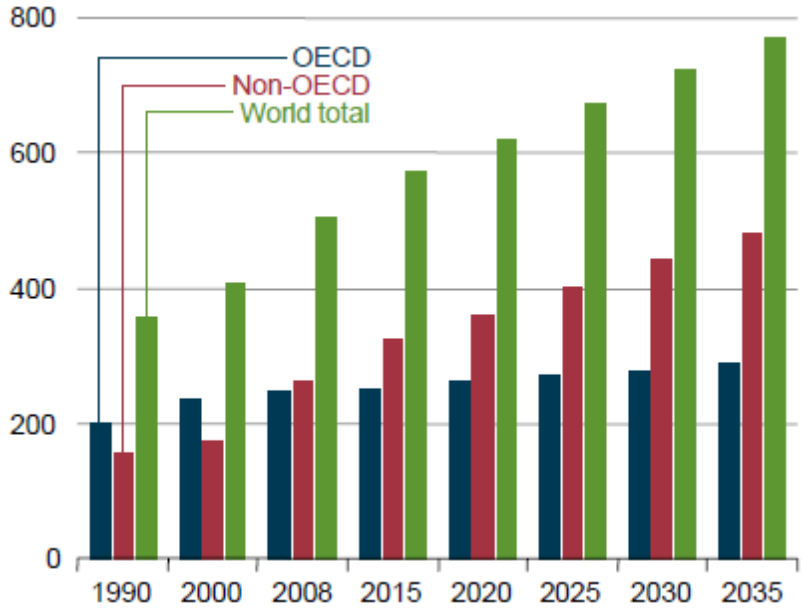

Fig. 1.1 World energy consumption 1990-2035 (quadrillion Btu) [1.1]

Today a large proportion of energy is supplied by burning fossil fuels like oil, coal, and natural gas (Fig. 1.2). It is officially agreed that combustion of fossil fuels is the main reason of global warming. In IPCC report [1.2] the correlation between the increase of the global temperature and the increase of anthropogenic emitted greenhouse gases was proven on a scientific base. With a share of 70% of the so called greenhouse effect, carbon dioxide takes up an exceptional position under the greenhouse gases. According to the fourth IPCC-Report, "Carbon dioxide is the most important anthropogenic greenhouse gas produced by combustion of fossil raw materials.

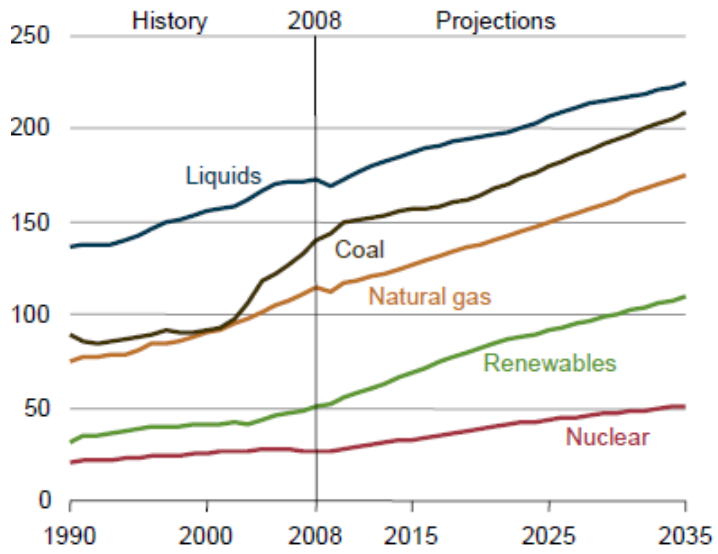

Fig. 1.2 World energy consumption by fuel 1990-2035 (quadrillion Btu) [1.1]

It is predicted by the United Nations Intergovernmental Panel on Climate Change that the warming of the Earth over the next 50 years could induce glacial melting, raise sea level and change weather patterns.

Therefore, to alleviate the threat from such environmental catastrophes and to maintain our planet inhabitable for other generations it is necessary to diversify our energy portfolio as early as possible, using renewable energy such as solar energy, wind power, and geothermal energy that do not release greenhouse gases.

According to Fig. 1.3 the amount of energy which Earth surface receives from the sun is around 89000 TW, while world energy consumption converted into power is equal to 15TW [1.3]. Therefore, it is clear that utilization of a minuscule fraction of solar power coming to the Earth is enough to meet our global energy demands. This fact shows what enormous potential sun energy would have for our energy balance if it could be efficiently collected. There are three main types of solar energy collectors: solar thermal collectors, concentrating solar power plants and photovoltaic devices. Photovoltaic (PV) solar cells show the most promising prospects in exploiting this inexhaustible power source.

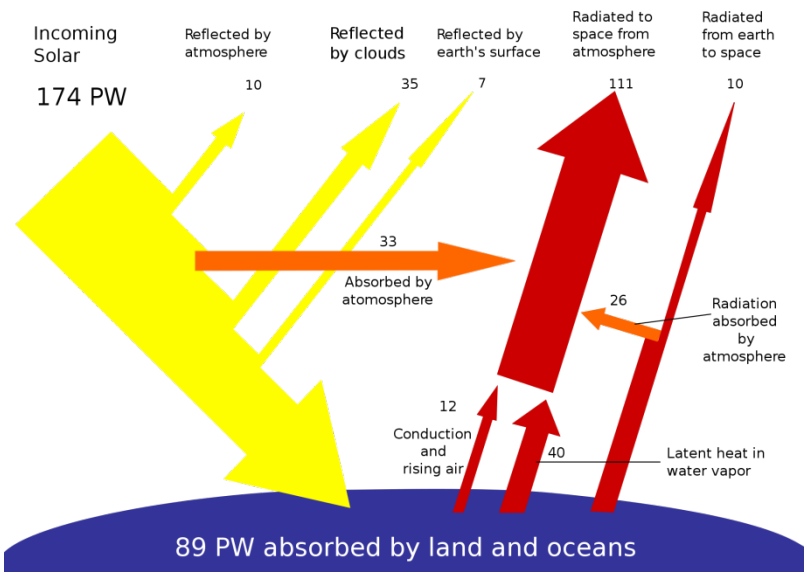

Fig. 1.3 Breakdown of the incoming solar energy

PV solar cells are electronic devices that convert incident solar radiation directly into electricity. In doing so, solar cells generate electricity without releasing carbon dioxide or other greenhouse gases into the atmosphere. For this reason, it is accepted as an ecologically superior electricity generating technology. Since sunlight shines everywhere on the Earth PV solar cells posses a very desirable advantage of being able to be used everywhere despite the geographical location. This feature benefits people living in the rural or mountainous areas of developing countries in particular. Two and a half billion people live in these areas without access to electrical grid, because it is too expensive to distribute electricity to them by conventional means (i.e., by extending transmission lines from a centralized power station) [1.4]. In addition, PV-generated electricity is also a very secure means of power generation, because it is not involved in any competition of fuel sources and transportation of fuels. For these reasons, PV applications have experienced a spontaneously exponential growth since the late 1970s. The global installed base of PV generation had exceeded 1 GW by the year 2000 and over 24 GW of PV installations at the end of year 2011[1.5]. Although photovoltaic solar cells are being more and more accepted as a viable means of electricity generation, high price and expectations for more efficient cell in the future prevent PV industry from even faster growth.

Solar cell metallization is one of a major efficiency-limiting and cost-determining step in solar cell processing. The most efficient technique is Photolithography (PL) which allows achieving

very low metal contact resistance, narrow gridlines and virtually no junction shunting, resulting in the highest fill factors and cell performance. Buried contact solar cells (BCSC) are representatives of high efficiency devices. Characteristic for this technology is that the front contacts are placed in deep trenches, formed by laser. The result is minimized width of the contact bars due to increased depth of the contact. In this way the formed element has lower shadowing effect and additionally the contact resistance is decreased.
In industrial mass production the screen-printed (SP) solar cell is the most common type of solar cell fabricated. Screen printing technology is robust, generates low amount of chemical wastes and the production process can be easily automated because of its simplicity. Despite its popularity, SP technology is far from being optimal in metallization. Although screen printing technique is applied to solar cells since the 1970s, the understanding of the silver thick-film contact to the emitter of a solar cell is still controversial. Currently, most of metallization properties that yield the best cell efficiency are determined empirically which may not represent the highest achievable cell performance. There is a big gap between efficiency of photolithography and screen-printing techniques motivating to do more research in this field and try to get SP closer to PL. To achieve this, the understanding of contact formation must be realized and after that the production process could be optimized. This would significantly increase solar cell efficiency and reduce its costs helping photovoltaic energy to reach grid parity.

The goal of this work was to improve understanding about front side metallization process by using correlation between structural and electronic properties of different solar cell regions. In order to achieve this, several solar cells were fired at different peak temperatures to find optimal firing temperature. As a result, under fired, over fired and optimally fired cells were processed. Sufficient information about electronic properties was obtained from IV curves and series resistance maps. Electron microscopy was performed to collect data about structural properties of samples fired at different temperatures and showing different series resistances. TEM was used to investigate metal/semiconductor interfaces of under fired, over fired and optimally fired cells.

Finally, it is necessary to mention that this thesis deals only with front side metallization process as this part is more important for efficiency enhancement and has more questions to be answered. From now on, all definitions of metallization, screen-printing and contact formation will be related only to front side metallization unless stated otherwise.

This work consists of four main sections. First of all, the basic theory about solar cell working principles, metallization process and transmission electron microscopy is introduced in chapter 2. Secondly, experimental equipment and procedure are described in chapter 3. Thirdly, the results are being presented and discussed in chapter 4. Finally, conclusions are made in chapter 5.

2. Theory

2.1 Solar cell basics

In this chapter principles of solar cell technology will be introduced. Process of how solar cell becomes an electricity generating device from bulk semiconductor material will be discussed. Finally, main solar cell parameters will be explained. This chapter is mainly based on text from references [2.1, 2.2, 2.3 and 2.4].

2.1.1 Solar spectrum

All electromagnetic radiation, including sunlight, is composed of particles called photons which exhibit wavelike properties as well. Each of them carries a specific amount of energy, E_λ depending on their wavelength:

$$E_\lambda = \frac{hc}{\lambda}; \quad (2.1)$$

where h is Planck's constant, c is the speed of light and λ is the wavelength.

The sun has a surface temperature of 5762 K and its radiation spectrum can be approximated by a black-body radiation law. The sun emits great amounts of energy, but due to the Earth's great distance from the sun it receives only a small fraction of this energy. For the same reasons, only those photons emitted directly towards the Earth contribute to the solar spectrum. The solar constant is the amount of power that the Sun deposits per unit area that is directly exposed to sunlight. The solar constant is equal to approximately 1,368 W/m^2 just above the Earth's atmosphere and this spectral distribution is referred to Air Mass zero (AM0) radiation spectrum. Sunlight on the surface of Earth is attenuated by the Earth's atmosphere and the power density of 1,000 W per square meter is received in clear conditions when the Sun is near the zenith - Air Mass 1.5 spectrum (Fig 2.1).

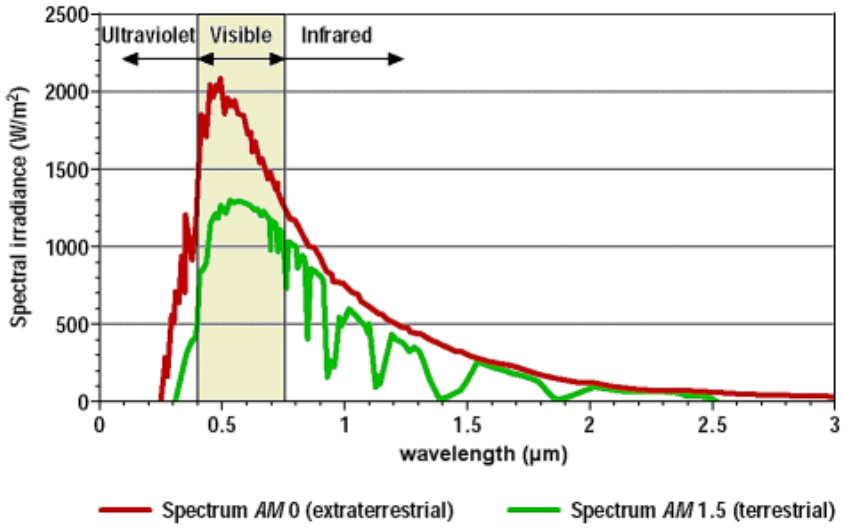

Fig. 2.1 Comparison of AM0 and AM1.5 spectra [2.4]

2.1.2 Semiconductor material

Solar cells can be fabricated from various semiconducting materials. Most common is silicon (Si) due to the fact that it is one of the most abundant materials on the Earth; its manufacturing technology is very well developed and cheap because of wide use in electronics industry. Despite that, Si has some strong disadvantages like band gap value of 1.1 eV which is slightly lower than optimal (1.4 eV) and low absorption coefficient mainly due to indirect band gap. To overcome these drawbacks scientists use semiconductor compounds like GaAs, GaInP, $Cu(InGa)Se_2$, CdTe etc. or amorphous silicon for solar cells. However, these alternatives still suffer from high costs, possible material shortage under the case of mass production (tellurium), toxicity etc.

To understand how solar cell works some fundamental solid state physics will be explained in the subsequent paragraphs. As this thesis is directed towards Si solar cells and it is the most common material in solar cell industry all examples will be related to silicon.

2.1.3 Properties of semiconductors

Semiconductor is a solid state material with many atoms arranged in an ordered way. This arrangement causes a solid material to have continuous energy bands instead of discrete energy levels as single atoms have. The energy distribution of the bands depends on the electronic properties of the atoms and the strength of the bonding between them. The highest occupied band, which contains the valence electrons, is called the valence band. The lowest unoccupied

band is called the conduction band. In semiconductors the valence band is completely full and separated from the conduction band by an energy gap called band gap. The band gap of semiconductors is in the range of 0.5 to 3.0 eV. There are two types of band gaps: direct and indirect (Fig. 2.2). When the minimum of the conduction band occurs at the same value of the crystal momentum as the maximum of valence band the semiconductor is a direct band gap semiconductor. If they appear at different value of the crystal momentum then semiconductor has an indirect band gap.

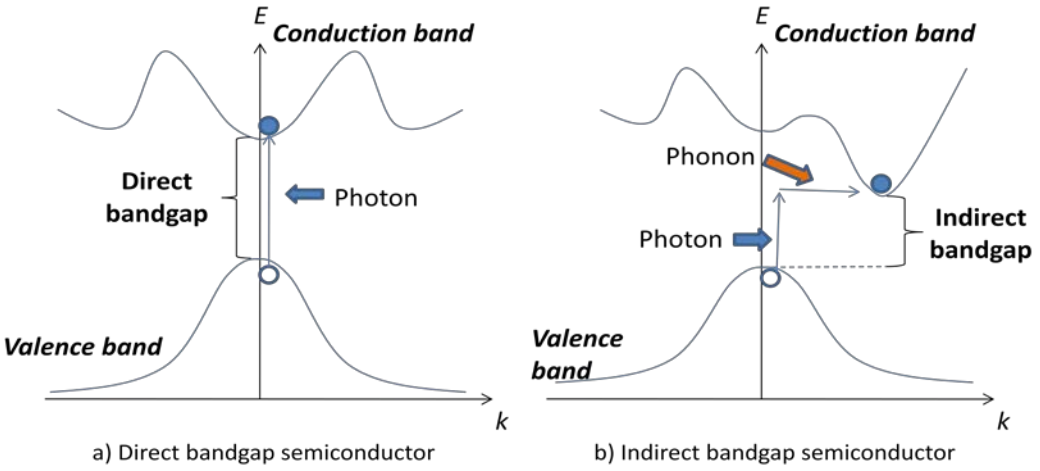

Fig. 2.2 Example of energy band diagrams of direct and indirect band gap semiconductors

The energy distribution of the electrons determines which of the states in the conduction band are filled and which are empty. This distribution is described by Fermi-Dirac statistics. *f(E)* is the probability that a level with energy E will be filled by an electron, and the expression is:

$$f(E) = \frac{1}{1+\exp\left((E-E_F)/k_BT\right.}. \qquad (2.2)$$

where k_B is Boltzmann's constant, $8.62 \cdot 10^{-5}$ [eV/K], T is the temperature in degrees Kelvin and E_F is Fermi level which is defined as the energy point where the probability of occupancy by an electron is 50%. At absolute zero temperature, no conductivity is available because probability for electron to occupy conduction band is zero. As the temperature is raised, the electrons gain kinetic energy from lattice vibrations and are able to reach conduction band.

2.1.4 Doping

Semiconductor material which has no impurities added to it in order to change the carrier concentrations is called intrinsic material. The number of electrons in the conduction band and holes in the valence band is equal. The intrinsic carrier concentration is typically very small compared to the densities of states (for example, the generally accepted value for the intrinsic carrier concentration of silicon, n_i, at 300 K is 1.01 x 10^{10} cm^{-3}) and intrinsic semiconductors behave like insulators. This problem is solved by doping semiconductor with specific impurities. Impurities can be donors and acceptors. The introduction of donor and acceptor impurities into a semiconductor allows the creation of the n-type (electrons are the primary charge carriers) and p-type (holes are the primary charge carriers) semiconductors, respectively. With a large number of dopants the semiconductor conductivity is sufficiently enhanced.

2.1.5 Light absorption and charge carrier generation

So far a semiconductor at equilibrium was considered which means that there is no current flowing. To make a solar cell operate it is necessary to disturb it from equilibrium. It happens when photons are absorbed which create electron-hole pairs. However, total energy and momentum of all particles involved must be conserved. This means that in direct band gap semiconductors photons need to have energy higher than band gap to excite electrons to conduction band. On the other hand, in indirect band gap semiconductors energetic photon as well as phonon (particle representing lattice vibration) is necessary for electron excitation to satisfy both conservation laws. As a result, absorption of indirect band gap semiconductors is less probable than direct band gap semiconductors.

The ability to absorb photons can be related to absorption coefficient. It determines how far into a material light of a particular wavelength can penetrate before it is absorbed. The absorption coefficient, α, depends on the material and also on the wavelength of light which is being absorbed and can be calculated by using following formula:

$$\alpha = \frac{4\pi k}{\lambda}; \tag{2.2}$$

where $\underline{\lambda}$ is the wavelength and k is extinction coefficient (or imaginary part of refractive index). Because of absorption, light travelling through material is being attenuated. The intensity of light at any point in the material can be calculated according to the equation:

$$I = I_0 e^{-\alpha x}; \quad (2.3)$$

where α is the absorption coefficient typically in cm^{-1}, x is the distance into the material at which the light intensity is being calculated; and I_0 is the light intensity at the top surface. This equation shows that most of the photons are being absorbed at the surface of solar cell, and light intensity decreases exponentially as it goes deeper into material.

The number of electrons generated at each point in the device due to the absorption of photons is called generation rate. Assuming that the loss in light intensity is directly related to absorption of photons and generation of an electron-hole pair, then the generation G in a thin slice of material is determined by finding the change in light intensity across this slice. Consequently, differentiating the above equation will give the generation at any point in the device. Hence:

$$G = \alpha N_0 e^{-\alpha x}; \quad (2.4)$$

where N_0 is photon flux at the surface; α is absorption coefficient; and x is distance into the material.

2.1.6 Charge separation

There are several ways of making charge separating mechanism but the classical model is p-n junction. It is made when p-type semiconductor is placed in contact with n-type semiconductor. Then a diffusion of electrons occurs from the region of high electron concentration (the n-type side of the junction) into the region of low electron concentration (p-type side of the junction). When the electrons diffuse across the p-n junction, they recombine with holes on the p-type side. As atoms on n-type semiconductor are losing and atoms on p-type semiconductor are gaining electrons they become positive and negative ions and create an electric field. This electric field promotes charge flow, known as drift current that opposes and balances out the diffusion of electrons and holes. This region where electrons and holes have diffused across the junction is called the depletion region because it no longer contains any mobile charge carriers. P-N junction in thermal equilibrium is depicted in Fig. 2.4.

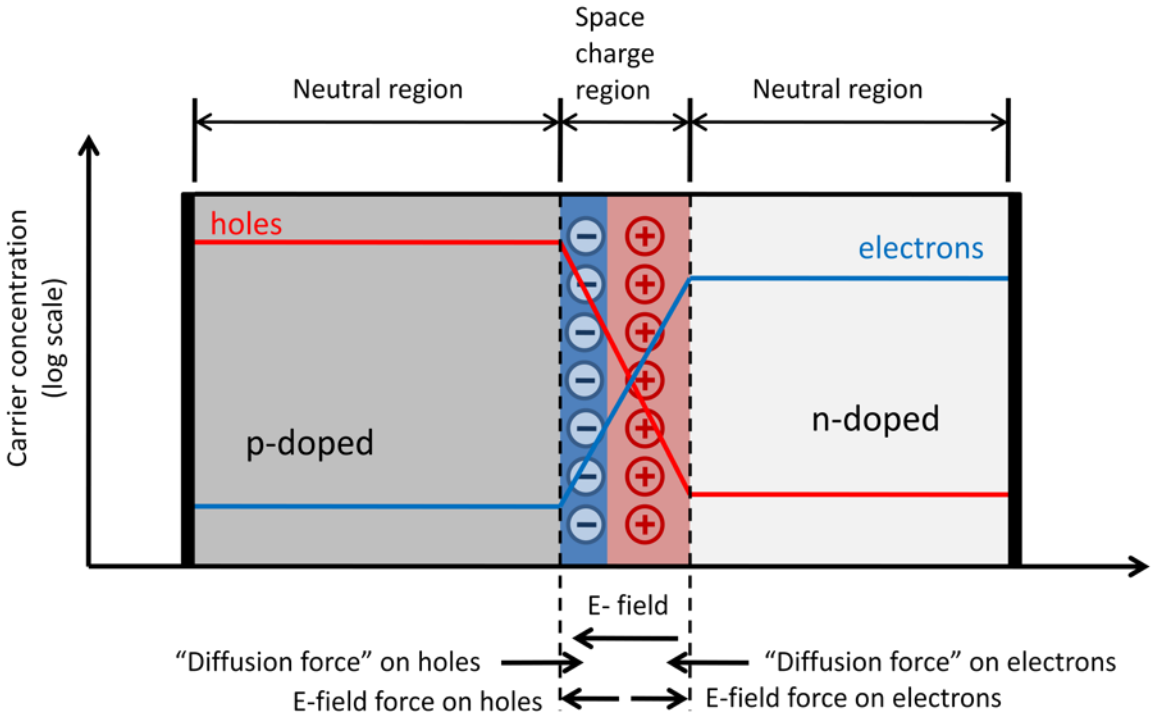

Fig. 2.4 P-N junction in thermal equilibrium

To use p-n junction as solar cell we need to make contacts on both n and p type semiconductors and connect to a circuit with external load. As we know from previous chapter, semiconductor could be disturbed from equilibrium by exposing it to light. Electrons that are created on the n-type side, or have been "collected" by the junction and swept onto the n-type side, may travel through the wire, power the load, and continue through the wire until they reach the p-type semiconductor-metal contact. Here, they recombine with a hole that was either created as an electron-hole pair on the p-type side of the solar cell, or a hole that was swept across the junction from the n-type side after being created there. This sequence of solar cell powering the external load is shown in Fig. 2.5.

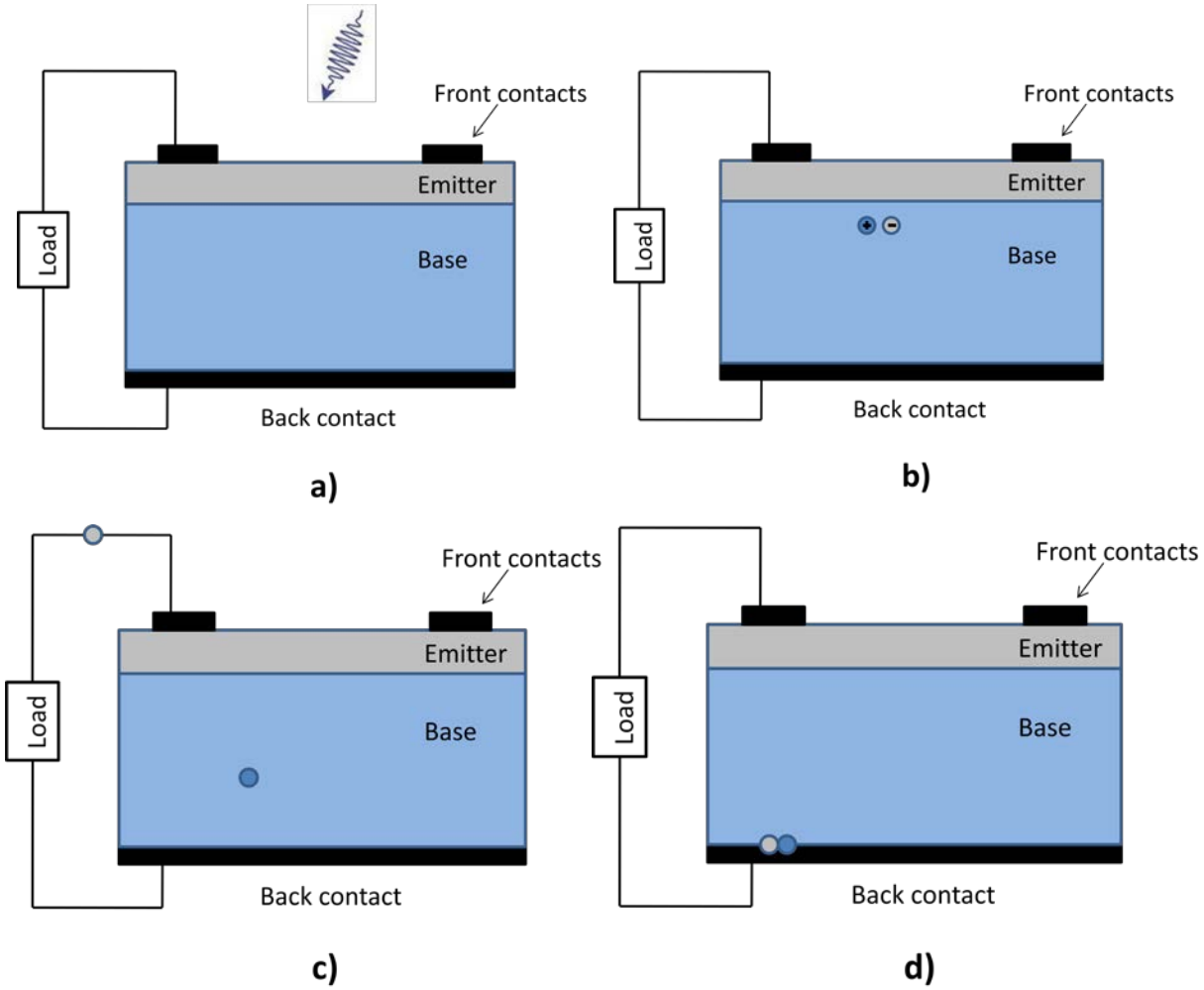

Fig. 2.5 a) a beam of light shines on a solar cell; b) electron-hole pair is generated at the bulk of a solar cell; c) electron is swept to n-type semiconductor by electric field and travels through the wire, while hole is diffusing towards back contact; d) electron after powering external load recombines with hole [2.4]

2.1.7 Solar cell parameters

Up to now, solar cell, capable of powering external load, was described. However, of equal importance is to know the quality of performance of this solar cell. Therefore, the most important parameters of solar cell will be introduced in this paragraph.

PV cells can be modeled as a current source in parallel with a diode. When there is no light present to generate any current, the PV cell behaves like a diode. As the intensity of incident light increases, current is generated by the PV cell. Solar cell performance can be expressed as following equation:

$$I = I_l - I_o\left(e^{\frac{q(V+IR_S)}{kT}} - 1\right) - \frac{V-IR_S}{R_{sh}}; \quad (2.5)$$

where I_l is current generated by photoelectric effect, I_o is the saturation current of the diode, q is the elementary charge 1.6x10^{-19} Coulombs, q is a constant of value 1.38x10^{-23}J/K, T is the cell temperature in Kelvin, V is the measured cell voltage, R_S and R_{sh} are series and shunt resistances.

The current dependence on voltage or IV characteristic is a visual representation of equation 2.5 and gives many performance parameters. The example of IV curve is plotted in Fig. 2.6.

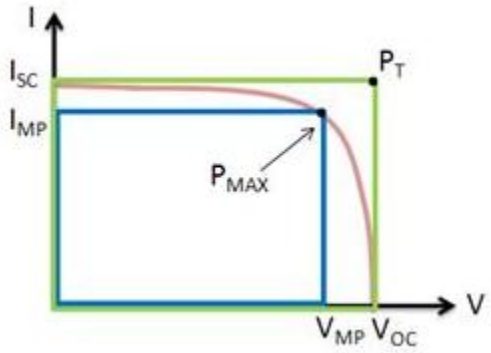

Fig. 2.6 Example of IV curve with most important parameters identified on the graph

When the contacts are isolated (I=0), the potential difference has its maximum value, open circuit voltage Voc:

$$V_{oc} = \frac{kT}{q}\ln\left(\frac{I_{sc}}{I_0} + 1\right); \quad (2.6)$$

When the contacts are connected (V=0) a short circuit current I_{sc} is drawn.

The power produced by the cell can be easily calculated by the equation $P=IV$. At the I_{SC} and V_{OC} points, the power will be zero and the maximum value for power will occur between the two. The voltage and current at this maximum power point are denoted as V_{MP} and I_{MP} respectively.

The Fill Factor (FF) is essentially a measure of quality of the solar cell. It is calculated by comparing the maximum power to the theoretical power (P_T) that would be output at both the open circuit voltage and short circuit current together.

$$FF = \frac{P_{MAX}}{P_T} = \frac{I_{MP}V_{MP}}{I_{sc}V_{oc}}; \tag{2.7}$$

The efficiency, η, of the cell is the ratio between power density delivered at operating point, P_{MAX}, and the power density of incident light, P_{in}.

$$\eta = \frac{P_{MAX}}{P_{in}}; \tag{2.8}$$

During operation, the efficiency of solar cells is reduced by the dissipation of power across internal resistances. These parasitic resistances can be modeled as a parallel shunt resistance (R_{SH}) and series resistance (R_S). For an ideal cell, R_{SH} would be infinite and would not provide an alternate path for current to flow, while R_S would be zero, resulting in no further voltage drop before the load. Decreasing R_{SH} and increasing R_s will decrease the fill factor (FF) and P_{MAX} as shown in Figure 2.7. If R_{SH} is decreased too much, V_{OC} will drop, while increasing R_S excessively can cause I_{SC} to drop instead.

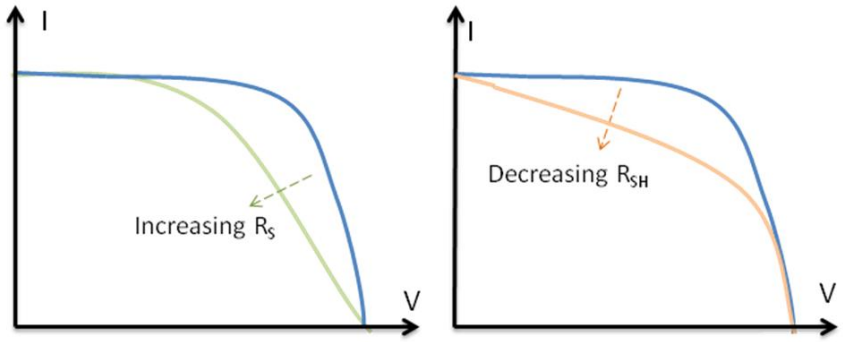

Fig. 2.7 Effect of series and shunt resistances on solar cell quality

2.2 Metallization

In subsequent chapters different technologies being used for the metallization process are reviewed, current transport models of screen printed contact are presented and theoretical contact formation process is proposed.

2.2.1 Metallization technologies

The process of front contact formation is one of the most important solar cell processing steps. The main function of front contacts is to collect current therefore series resistance losses must be minimal. However, contacts have a negative property of shadowing the cell so they must cover as less front cell area as possible. The applied metallization technique also determines the emitter diffusion profile, surface doping concentration and the choice of certain surface passivation techniques. In order to meet these requirements, several techniques are implemented in solar cell production.

The **buried contact** solar cell was developed at the University of New South Wales as a high-efficiency metallization technique. Using this method, solar cells of high quality contacts with low shadowing losses and low contact resistance are fabricated. The main advantages of BCSC include:

- High transparency due to narrow metal lines (fingers)
- Low finger resistance due to the high metal aspect ratios (ratio of depth and width of the finger)
- Low contact resistance given by large metal/silicon interface
- Low emitter resistance caused by close spacing of metal grid lines
- Good blue response through the use of a lightly doped emitter

The buried contact technology overcomes many of the disadvantages associated with screen-printed contacts and this allows buried contact solar cell to achieve higher efficiencies. A performance study performed by Mason and Jordan [2.5] shows that buried contacts achieve 20% to 30% better results than screen-printed solar cells. The highest efficiency reported on BCSCs under one sun illumination is 20.6% using FZ-Si on a cell area of 12 cm^2 [2.6].

The production sequence for laser grooved buried contact solar cells starts with removal of damaged outer layer of silicon by using strong alkaline solution. This is mainly mechanical damage caused by the saw when the silicon crystal is sawed into wafers. The wafer has a high reflectivity after etching. This problem is solved by texturing the wafer. To form p-n junction wafer is heated in a furnace at 800-1000 degrees with a phosphorus atmosphere. Phosphorus diffuses into the surface and forms n-type layer. Heating the wafer to a high temperature in the presence of water vapor causes the outer layers to oxidize and turn into silicon dioxide. Then a series of grooves are cut in the top surface of the wafer with either a laser or a mechanical saw (about 30μm wide and 80μm deep). A second phosphorous diffusion is performed to get p-n junction in the grooves. The oxide layer works as a mask and confines phosphorous to the grooves. Then back surface aluminum contact is formed and then thin barrier layer of nickel and copper is plated to exposed areas of silicon. Copper completely fills the grooves and coats the back surface. After edge isolation the cell is ready to use (Fig. 2.8).

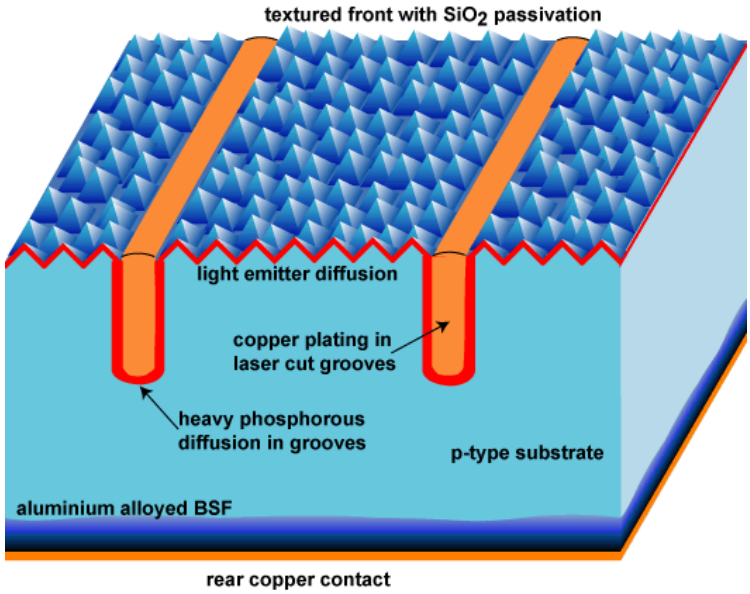

Fig. 2.8 Cross-section of laser grooved buried-contact solar cell [2.4]

The main problem related to this technology is an environmental issue. The external costs of meeting environmental specifications of developed countries with processes producing an enormous amount of rinse water containing nickel and copper must be taken into account. It can be a major issue for planning large volume plants above 100MW.

Photolitography (PL) and metal evaporation is most established metallization technique obtaining highest efficiencies. This method is widely used in electronics industry, especially in forming integrated circuits. With the photolithography and evaporation process, well defined contacts of very fine dimensions can be produced. Contacts made using this technique have very low metal contact resistance (1×10^{-5} mΩ-cm^2)[2.7], very narrow gridlines (~8 μm) and virtually no junction shunting, resulting in the highest fill factors and cell performance. Efficiencies of 24.7% on single crystal Si and 20.3% on cast multicrystalline Si have been recorded with PL contacts [2.8, 2.9, 2.10].

The production process consists of the following steps. First a photoresist is deposited on the front using the spin-on technology and dried to drive out excess solvents. A mask with the desired front side structure is placed on top of the resist and illuminated. The illuminated areas of the photopositive resist become soluble and can be washed out using a developer solution. Typically the wafer is then “hard-baked” to solidify the resist to make it more stable for the following wet chemical etch process of the SiN_X and/or SiO layer. In the subsequent high vacuum evaporation process the metal or a stack layer of metals is deposited on the front. A common stack system is titanium palladium silver. Titanium forms a relatively low contact resistance of less than 10^{-5} W cm² to an n-doped emitter with a surface doping concentration above $1\cdot10^{19}$ cm^{-3}. In addition titanium reduces the native silicon oxide and forms a contact of good adhesion. Palladium is used as diffusion barrier and adhesion promoter between titanium and silver. The top silver layer is used as conductor to transport the current as loss-free as possible to the busbars. In a last step the rest of the photoresist covered by the excessive metal is removed in the lift off process. Solvents like acetone penetrate into the very thin metal layer at the edge of the resist openings. As a consequence a reaction with the resist occurs and the resist and the excessive metal can be lifted off. The thin metal stack system is typically thickened by a silver plating step and sintered. Simplified process is sketched in figure 2.9.

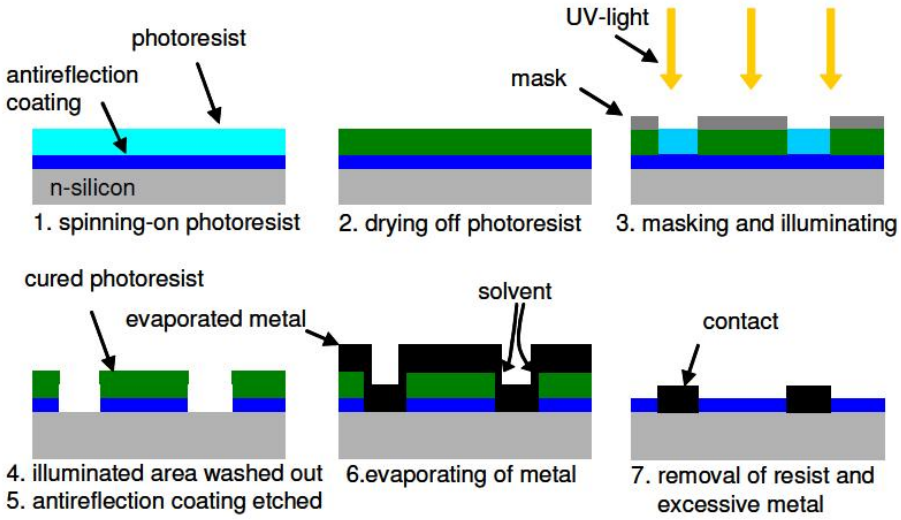

Fig 2.9 Photolithography and evaporation process sequence for metallization process on silicon solar cell

Despite superb performance of pholithographycally metalized solar cells, this technology is time-consuming and expensive due to the use of photo-resist mask patterning and vacuum evaporation of metals. This has lead to the development and use of simpler metallization techniques in production.

Screen-printing is the most mature and very well established solar cell fabrication technology and screen-printed solar cells currently dominate the market for terrestrial photovoltaic modules. This contact formation technique is more rapid and cost-effective compared to photolithography and buried-contact techniques. The screen-printing equipment is robust, simple and inexpensive, and the technique can be easily automated. Another big advantage is the potential of this technology. Despite the fact that screen-printed cells are least efficient when compared with two techniques mentioned above they still take the largest part of metallization industry market and the idea that it could be improved even more makes this technique a very attractive field of research. As this work is mainly focused on screen-printing technique, a more thorough explanation of it will be presented in the next chapter.

There are more metallization technologies like stencil-printing, pad-printing, ink-jet printing or dispensing, however they are used on lab scale only and are mainly derivatives of other techniques so are not described in detail in this work.

2.2.2 Screen-printing technology

In mass production the screen-printed solar cell is the most common type of solar cell fabricated. The process of such a cell production is simple and reminds that of buried-contact process except of a few steps.

First of all, a starting p-type boron doped (10^{16} cm^{-3}) wafer is processed in etching solution to remove saw damage. To increase absorption, the front side is textured using an acid solution in case of multicrystalline wafers or an alkaline solution in case of monocrystalline wafers. Afterwards wafer is exposed to phosphorus gas at high temperatures which results in phosphorus diffusion to the surface and n-type layer formation. An improved irradiation absorption and surface passivation is achieved by applying a SiN antireflection coating by PECVD (plasma enhanced chemical vapor deposition) or sputtering technology [2.11]. Metallization starts with printing rear side contacts then continues with printing front side contacts and finishes with a firing step. Contact material is printed on wafer in a desirable pattern using a special screen. The rear side is completely covered by an aluminum paste except of two busbars along the wafer which are printed using Al/Ag paste to make contact solderable. Aluminum is used because it forms a good ohmic contact with silicon. The paste is a viscous liquid due to the solvents it contains so it needs to be dried before proceeding to the next steps. Drying is performed in an in-line furnace at 100-200^{o}C. The same operations are performed for front side metallization. However, a screen with a different pattern of lines is used to avoid shading effect. A final step of contact firing at high temperatures is needed to evaporate organic components of the paste, sinter metallic grains together to form a good contact and to form a good electric contact with silicon. During firing, the active component of the front paste must penetrate the anti-reflection coating (ARC) to contact the n-emitter without shorting it: too mild heat treatment will render high contact resistance, but too hot or too long firing can cause the silver to etch through emitter and contact the base resulting in small shunt resistance. The back paste, on the other hand, must completely perforate the parasitic back emitter to reach the base and form so called back-surface field (BSF). A "back surface field" (BSF) consists of a higher doped region at the rear surface of the solar cell. The interface between the high and low doped regions behaves like a *p-n* junction and an electric field forms at the interface which introduces a barrier to minority carrier flow to the rear surface. The minority carrier concentration is thus maintained at higher levels in the bulk of the device and the BSF has a net effect of passivating the rear surface [2.12].

After phosphorus diffusion the wafer is completely covered with n-type layer. Back side layer is removed during firing, but the sides are still working as shunting paths. Therefore, they need to be removed as well (edge isolation). There are two different ways to do this:

- When plasma etching method is used, the cells are coin-stacked and placed into barrel-type reactors. In this way the surfaces are protected and only the edges are exposed to the plasma. A fluorine compound is excited by RF field and forms highly reactive species which quickly etch the exposed silicon surface.
- Laser cutting of the wafer edges is an alternative for plasma etching.

After edge isolation cell is ready to test and mount into module. Even though screen-printing is simple and easy technique to use, there are elements and steps in the process which must be handled very carefully. Firstly, screens and pastes which are necessary for this technology.

Screens. Screens are tight fabrics of synthetic or stainless steel wires stretched on an aluminum frame (Fig. 2.10). The screen is covered with a photosensitive emulsion, which is treated with photographic techniques in such a way that it is removed from the regions where printing is desired. To print fine but thick contact lines, which are needed for solar cells, the wires must be very thin and closely spaced. In contrast, the opening of the reticule must be several times larger than the largest particle contained in the paste to be printed. Screens for solar cell production typically feature about 80 wires per centimeter, wire diameter around 10 μm, mesh opening around 30 μm, corresponding nearly 50% open surface that is not intercepted by wires. The screens are for multiple uses and it must be cleaned after use, because dried paste could clog the openings.

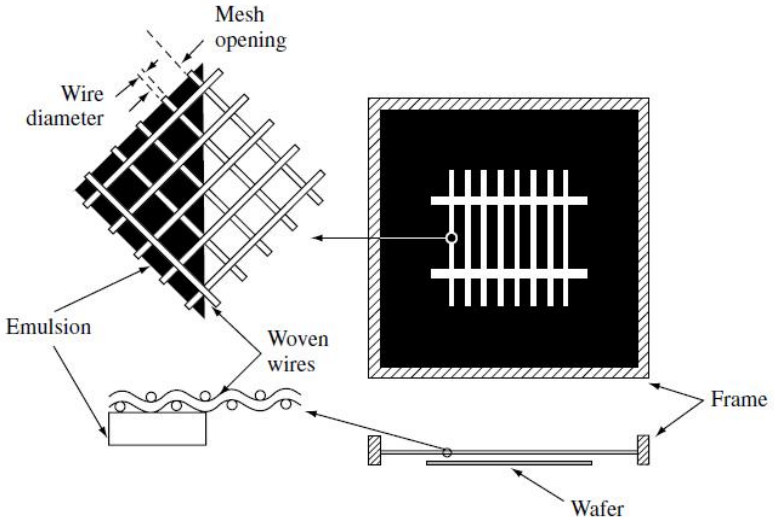

Fig. 2.10 A screen and a mesh used in screen printing technology [2.2]

Pastes. Mostly silver pastes are used for front side metallization. They generally consist of:

- Organic solvents and binders to make the paste fluid and hold all constituents together
- Conducting material for current collection which is silver powder composed of small (size of tenths of microns) crystallites
- Glass frit which is a powder of different oxides (lead, bismuth, silicon etc.) responsible for good quality contact between the silver fingers and the wafer.

The silver paste has to meet several requirements: etch away the ARC layer, form a contact with low contact resistance and support with a good adhesion properties which could guarantee that contact will not fall off during manufacturing process and period of operation.

Printing. The front contact is designed to collect current with minimum series resistance while minimizing optical shadowing. This means that contact area between silver and wafer must be as large as possible, but the covered wafer area by contacts should be as small as possible. Thus a compromise between the shadowing loss and the resistive loss is needed. High aspect ratio of contact fingers is a good solution to this problem, but is limited by the properties of the paste.
The screen and wafer are some distance apart called the snap-off. The paste is dispensed on the screen and squeegee made of rubber presses the screen and drags the paste along the screen. The paste penetrates through the openings in the screen and sticks to the wafer, forming a contact pattern. The amount of printed paste depends on the thickness of the screen material and the emulsion and the open area of the fabric. It also depends on viscosity of the paste. It must be fluid enough to fill all the volume allowed by the screen without voids. It must be viscous

enough not to spread over the wafer when printed. Snap-off distance, squeegee speed and pressure are critical parameters determining the height, the width and uniformity of the contact.

Firing. This step is performed in an in-line furnace with moving belt and usually consists of three parts. In the first part, at temperatures around 400^{o}C, the organic compounds are burnt off in the air. After that, the peak temperature of more than 800^{o}C is reached and contact formation takes place. Finally, the cells go out of the furnace and are cooled down in ambient atmosphere. A typical firing temperature profile is shown in figure 2.11.

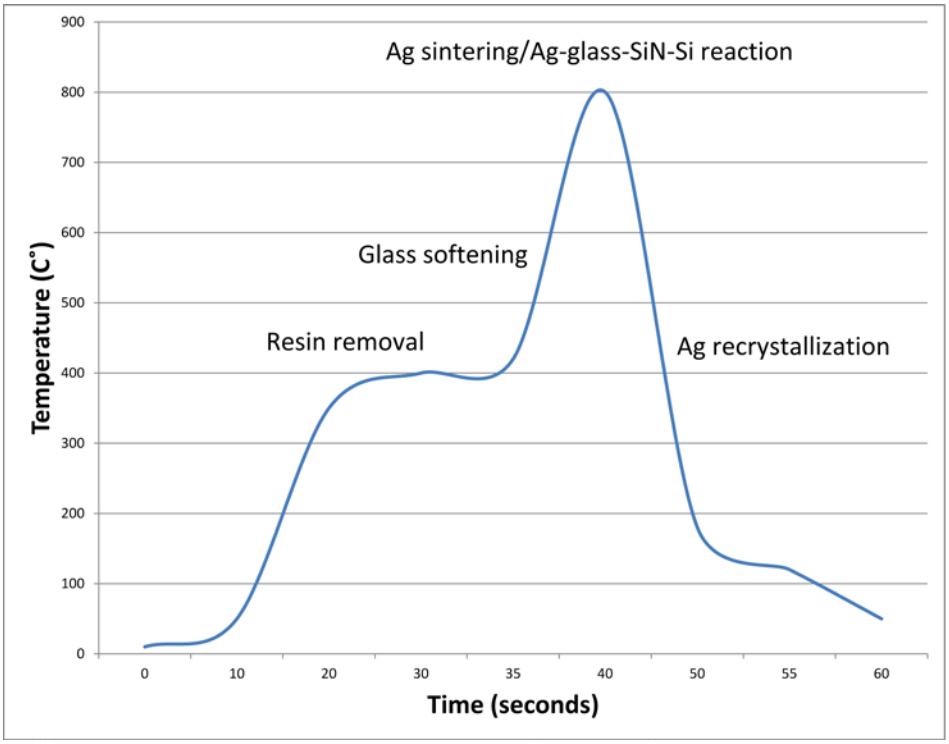

Fig. 2.11 A typical firing profile of crystalline silicon solar cell

Belt speed, firing temperature and firing profile are the most important properties which determine if the contacts are of good quality. If too low or too high peak temperatures are used, cells with large contact resistance are manufactured.

2.2.3 Contact formation model

During firing step a complex set of events happen to form a contact. A complicated interdependence of several parameters cause contact formation to be very difficult process to understand and explain. Therefore, various studies on different parameters must be performed to improve the existing knowledge about contact formation.

Despite previous work and studies, most of metallization parameters are determined empirically which may not be the most effective choice. New models, equipment improvements and novel ideas lead metallization process to a state where it is more based on science. There are several explanations on how atmospheric gases may influence the contact structure [2.13, 2.14]. The composition of silver paste is another important topic dealing with influence of different constituents [2.15, 2.16]. Firing parameters like peak temperature may be detrimental when quality of the contact is considered. Cooling rate is a crucial parameter which may change the overall structure of Ag/Si interface [2.16]. Finally, it is believed that solar cell performance might benefit from certainly oriented Si wafer as they get in better contact with the bulk silver [2.17].

The metallization of Si solar cells is simple to perform. Silver based printing pastes are commercially available. Screen-printing is a highly automated process and does not require highly skilled personal. Firing step is also easy to perform as cells just need to be passed through high temperature furnace in order to form a stable contact.

A typical silver thick-film paste consists of silver powder, glass frit, organic binder, solvent and certain additives to ensure proper printing properties. Usually a lead borosilicate glass with high lead oxide (PbO) content is used. When such paste is printed it sticks to the surface of the cell, but needs to be fired to get a good adhesion and conductive interface. Firing is performed in IR furnace at temperatures as high as 900˚C. During this process glass frit melts and etches through the antireflective coating making a way for the conductor particles to enable electrical contact to the emitter of the solar cell. On the other hand, glassy layer accumulates on the silicon surface and affects the current transport from the emitter to the bulk silver. At slightly higher temperatures the SiN layer is etched away and Ag particles tend to nucleate on the Si surface and form silver crystals.

According to Ballif [2.18] the Ag crystals are grown in pyramidal shapes and are distributed irregularly over the contact surface. He also found that the shape of the crystals can vary strongly as well. His study showed that glassy-layer/Si interface was lying some tens of nanometers below the initial Si layer which means that during the firing not only SiN is etched away but some Si as well. However, when Ag crystallites grow larger than 200 nm the orientation relation with the substrate is lost. Another interesting finding was that precipitates in glassy layer were

found only in over fired cells, and they mainly were lead particles. He concluded that these precipitates originate from etching the Si substrate through the following reaction:

$Si + 2PbO \rightarrow SiO_2 + 2Pb$ (**1**).

His investigation of electronic properties using Atomic Force Microscopy (AFM) showed a significantly low resistivity ($\rho_c \sim 2 \cdot 10^{-17} \Omega cm^2$) between the Si substrate and the crystallites when compared to typical macroscopic value of $10^{-3} \Omega cm^2$ for the entire contact. According to the author's calculations this macroscopic value would be reached if only 0.1% of the interface crystallites had a direct contact to the bulk Ag. Even though, such connections were not experimentally proven to exist they were expected to considerably contribute to the current flow. At locations where ultrathin glassy layer exists between the bulk Ag and the crystallites, tunneling current assisted by metal precipitates was expected to contribute to the current flow as well.

Schubert in his article [2.15] agreed that etching into silicon occurs via a redox reaction mentioned above. According to him, the reason why no metallic precipitates were found in optimally fired cells was that in the temperatures 600-700˚C silver is able to dissolve up to 5wt% lead. This also explains lead precipitates in over fired cells found by Ballif [2.18]. Schubert also states that pyramidal shape of many silver crystallites grown into [100] orientated silicon is a hint for epitaxial growth. He also concludes that two current paths are likely: direct crystallite-finger interconnection and multi-step tunneling process through thin glassy layer which was in agreement with Ballif.

The contact formation mechanism was proposed by Ballif in [2.18]. He states that upon heating, the glass frit melts, wets the wafer surface, etches the SiN layer and finally etches the Si substrate. In the process, excess Ag as well as etched Si are dissolved in the glass frit. During the cooling down phase in the over fired cells the excess Si contained in the glass frit recrystallizes epitaxially on the substrate and Ag crystallites grow randomly on the Si wafer. In optimally fired cells, Ag concentration is lower and crystallites grow in epitaxial relation with Si.

A more recent study by K.K. Hong [2.19] suggests a different explanation of contact formation process. First of all, an experiment of firing glass frit without silver powder showed a complete etching of SiN layer. This could be referred to the following reaction:

$$2PbO_{(in\ glass)} + SiN_{x(s)} \rightarrow 2Pb_{(l)} + SiO_{2\ (in\ glass)} + x/2N_{2(g)}\ \mathbf{(2)}$$

However, with addition of silver powder the chemistry was modified. The etching of the SiN layer by a mixture of glass frit and Ag powder was likely to occur through the following reaction:

$$2Ag_2O_{(in\ glass)} + SiN_{x(s)} \rightarrow 4Ag_{(s)} + SiO_{2\ (in\ glass)} + x/2N_{2(g)}\ \mathbf{(3)}$$

The reaction (1) responsible for Si wafer etching is gradually suppressed by reaction:

$$2Ag_2O_{(in\ glass)} + Si_{(s)} \rightarrow 4Ag_{(s)} + SiO_{2\ (in\ glass)}\ (4).$$

When the amount of Ag powder is small both reaction (**1**) and (**4**) can occur simultaneously. However, when Ag powder content reaches higher values the resulting liquid-Pb phase can redissolve into the glass through the following reaction:

$$Ag_2O_{(in\ glass)} + Pb_{(l)} \rightarrow 2Ag_{(s)} + PbO_{(in\ glass)}.$$

However, Ag paste containing more PbO in the glass frit showed increased reactivity with the SiN layer and the Si wafer. The paste containing less PbO in the glass frit was found to cause the Ag crystallites to be smaller and distribute more uniformly across the Si surface. Hong concluded that the solubility of Ag and viscosity of the glass frit are important factors controlling the size and distribution of the Ag crystallites at the glass/Si interface.

Separate studies held by Kontermann [2.13] and J.Y. Huh [2.14] examined the effect of nitrogen and oxygen gases on contact formation mechanism. Kontermann in his study shows that firing the contacts under nitrogen atmosphere causes an increase in series resistance. After structural investigations gaps around Ag crystallites were found. Gaps were expected to prevent current flow from the silicon into the silver crystal.

J. Y. Huh in his experiment [2.14] shows that an increasing partial pressure of oxygen gas significantly enhances the rate of Ag crystallite formation (Fig. 2.12). The sensitivity of the Ag crystallite formation to the O_2 gas suggests that this parameter may be used to improve contact quality.

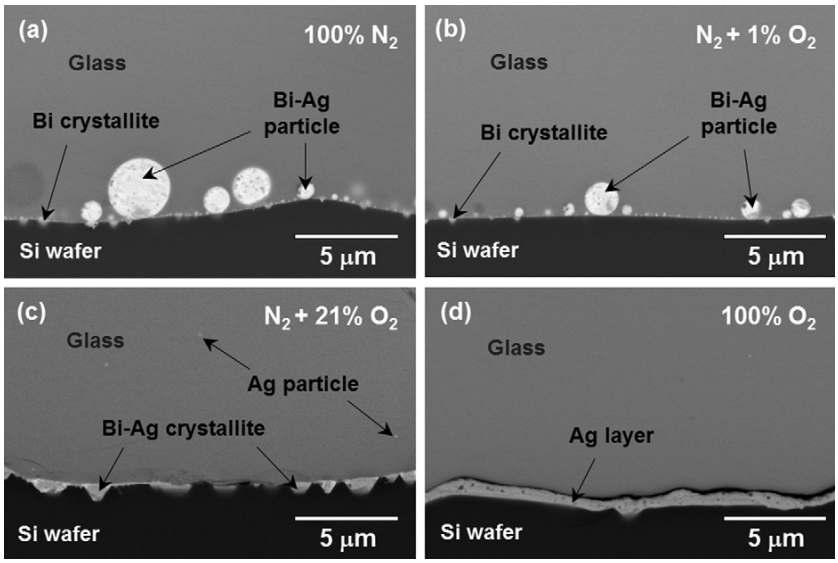

Fig. 2.12 Cross-sectional SEM micrographs after two steps of firing at 800 ◦C for 10 min. First, the glass frit alone was screen-printed on the Si wafer and fired at 800 ◦C for 10 min under the air (N2 + 21% O2) ambient. Then, Ag powder was screen-printed over the glass layer formed by the first firing and fired again at 800 ◦C for 10 min under various ambient conditions: (a) 100% N2, (b) N2 + 1% O2, (c) N2 + 21% O2, and (d) 100% O2 [2.14]

Another study by K. K. Hong [2.16] studied the Si/Ag interface after cooling the Si solar cells at different rates. After slow cooling in air atmosphere no Ag precipitates were detected in the glassy layer but Ag crystallites were apparent at the surface of the Si wafer. At fast cooling rates (cooling with ice water) Ag crystallites formed only at the apexes of the inverted pyramidal pits of the Si surface. Small spherical Ag particles were detected in the glassy layer. Accordingly, by varying cooling rate it would be possible to optimize the number and size of Ag crystallites together with silver precipitates in the glassy layer.

Finally, despite several studies supporting the hypothesis that Ag crystallites play an important role in current collection Z. G. Li came to a different conclusion in his study on multi-crystalline Si cells [2.20]. His TEM investigations aided by spatially resolved series resistance mapping showed that Ag crystallites are not absolutely needed for efficient current collection. His proposed model emphasizes the importance of photoelectrons collected through tunneling effect.

Many articles were written about contact formation and there are several models existing in the literature nowadays. It is generally agreed that the glass frit plays a critical role on front contact

formation. In [2.21] it is suggested that silver and silicon dissolve in glass frit during firing, but when cooling starts, Ag recrystallize on the surface of silicon wafer. These Ag crystallites are expected to work as current collectors and further current transport to the bulk of Ag finger takes place via tunneling. After summarizing the main studies on contact formation a general model can be introduced. The function of this model is to give a basic understanding of what is happening at Ag and Si interface during the firing step. Figure 2.13 shows a schematic representation of this model.

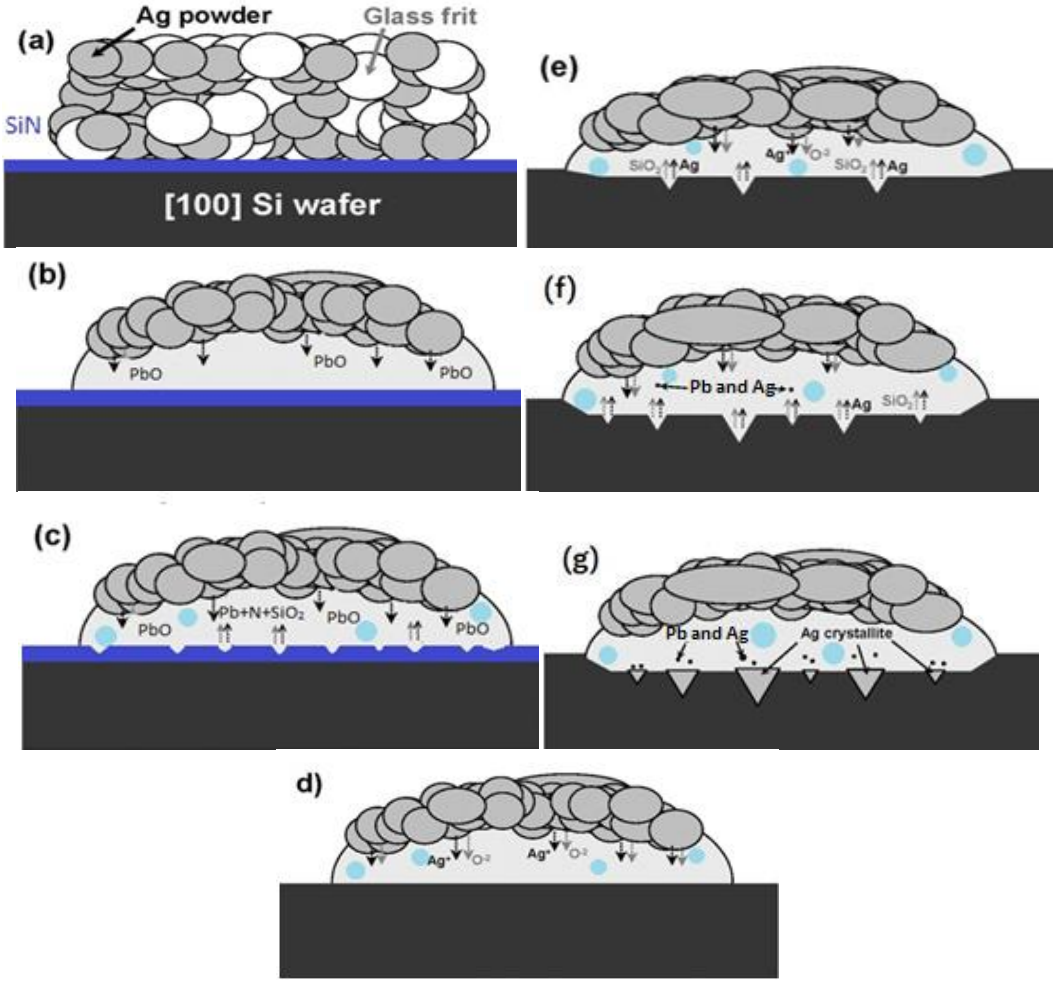

Fig. 2.13 Schematic representation of contact formation between Ag fingers and Si wafer (explanations in the text)

Before the final firing step, the Ag paste printed on the Si wafer is a random mixture of Ag powder and glass frit (organic solvents are already burnt out) (a). As temperature reaches glass softening point, the glass frit melts and wets Si surface. At slightly higher temperatures lead-

oxides start to dissolve into glass frit and diffuse towards Si (b). As PbO particles reach SiNx layer they start to etch it through the following redox reaction:

$$2PbO_{(in\ glass)}+SiN_{x(s)} \rightarrow 2Pb_{(l)}+SiO_{2(in\ \ glass)}+x/2N2_{(g)}.$$

The products of this reaction are liquid lead particles precipitating above Si wafer, silicon glass and nitrogen gas in a form of large pores (blue circles) in a glassy layer (c). At the same time some of Ag powder dissolves into the fluidized glass and the sintering of the Ag powder occurs. Some of these Ag atoms oxidize through an interaction with oxygen in the atmosphere through the following reaction:

$$4Ag_{(in\ glass)}+O_{2(g)} \rightarrow 4Ag^{+}_{(in\ glass)}+2O^{-2}_{(in\ \ glass).}$$

Both silver and oxygen ions diffuse toward Si wafer and helps etching SiNx layer. When SiNx is etched through, these ions etch small pits of specific shape (depending on surface orientation) into Si wafer (d,e). This happens via the following reactions:

$$2Ag_2O_{(in\ glass)}+SiN_{x(s)} \rightarrow 4Ag_{(s)}+ SiO_{2(in\ glass)} +x/2N_{2(g)}$$

$$4Ag^{+}_{(in\ glass)}+Si_{(s)}+2O^{-2}_{(in\ \ glass)} \rightarrow 4Ag_{(in\ glass)}+ SiO_{2(in\ \ glass).}$$

Finally, we have a glassy layer sitting on top of etched Si wafer with a lot of lead and silver particles precipitated near the wafer surface, nitrogen gas forms some pores and on top of glassy layer there is bulk Ag contact (f). When cells are out of the furnace and starts cooling, Ag precipitates crystallize into these pits which work as nucleation sites (g).

However, many aspects of the physics of the front-contact formation are not clear and further investigations are still needed for complete explanation of formation mechanisms.

2.2.4 Current transport mechanisms

Two main hypotheses on current transport mechanisms exist in literature (Fig. 2.14):

1. The glass layer at the interface is often assumed to be insulating and therefore responsible for high contact resistances. The current is consequently supposed to be transported via (local) direct interconnections between silver fingers and silicon. Some authors suggest [2.22, 2.23] that optimal fired contacts show direct silver–silicon interconnections that are not locally distributed but can be found over a large area.
2. Other scientists [2.24, 2.25] assume an increased tunneling probability in the glass layer due to dissolved silver. The current is supposed to be transported via a multi-step tunneling process from the emitter to the silver through the glass layer.

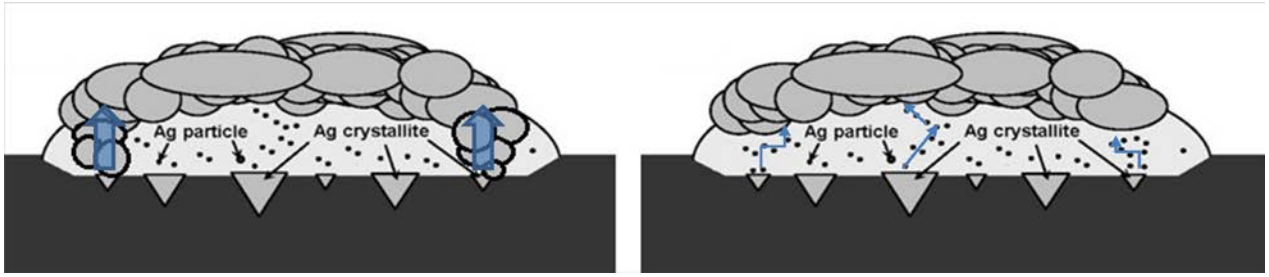

a) Direct b) Multi-step tunneling

Fig. 2.14 Schematic examples of direct (a) and tunneling (b) current transport mechanisms with suggested paths of current flow (blue lines)

2.2.5 Potential of screen-printing

There are few factors which tend to limit the solar cell performance:

- Screen-printed contacts are typically 125-150 μm wide, which increases shading losses
- High contact resistance, low metal conductivity and junction shunting causes low Fill Factors
- Effective emitter surface passivation is difficult because of the use of low sheet-resistance emitters with a high surface concentration.
- Poor blue-response due to heavy doping

These factors cause screen-printed cell to be 1.5-2% less efficient than cell with photolithography contacts. Fig. 2.15 shows quantitative breakdown of these losses and in table 2.1 differences in cell parameters are summarized [2.26].

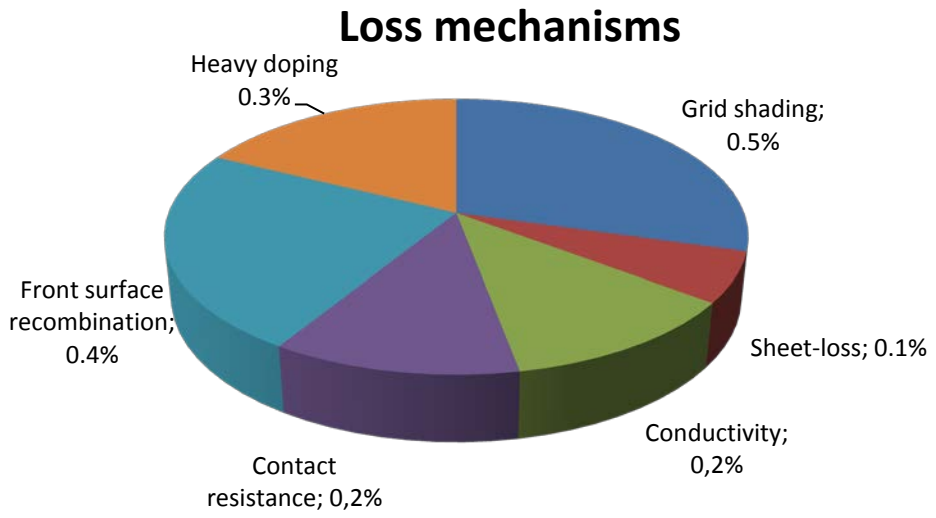

Fig. 2.15 Loss mechanisms in screen-printed cells relative to photolithography cells [2.15]

Parameter	**SP cell**	**BC cell**	**PL cell**
finger thickness	14 μm	50 μm	8 μm
finger width	80 μm	20 μm	20 μm
specific contact-resistance	0,3-3 mΩ/cm2	3 μΩ/cm2	0,01 mΩ/cm2
metal resistivity	3 μΩ/cm	1,7 μΩ/cm	1,7 μΩ/cm
Fill Factor	0,74-0,77	0,78-0,79	0,81-0,82

Table1. Comparison of contact parameters of screen-printing (SC), buried contact (BC), photolithography (PL) metallization techniques [2.15]

This chapter shows quantitatively how much potential screen-printing has. Better understanding of how paste and printing parameters influence contact quality would lead to higher efficiencies.

2.3 Introduction to transmission electron microscopy

To understand transmission electron microscopy it is necessary to understand types of electron scattering, diffraction phenomena, reciprocal space, and know what Ewald sphere and Bragg's law mean. In this paragraph the basics on these topics will be explained to construct a background which would help to understand the principles of transmission electron microscope. This section is mainly based on references [2.27, 2.28]

2.3.1 TEM resolution

Transmission electron microscopy (TEM) is a microscopy technique where a beam of electrons is transmitted through an ultra thin specimen, interacting with the specimen as it passes through. An image is formed from the interaction of the electrons transmitted through the specimen. The image is magnified and focused onto an imaging device, such as a fluorescent screen, photographic film, or to be detected by a sensor such as a CCD camera.

The resolution ρ of a microscope is defined as the distance between two details just separable from one another. It can be calculated using the Abbey theory of images formation for optic systems. For incoherent light or electron beam:

$$\rho = \frac{0.61\lambda}{\sin\alpha} \quad \text{(Rayleigh criterion)} \qquad (2.9)$$

where λ is the wavelength of the light, and α the maximum angle between incident and deflected beam in the limit of the lens aberrations. For optical microscopy, the resolution is therefore limited by the wavelength of light (410-660 nm). The X or gamma rays have lower wavelength, but unfortunately, high-performance lenses necessary to focus the beam to form an image do not exist yet. In 1923, De Broglie showed that all particles have an associated wavelength linked to their momentum: $\lambda = h/mv$ where m and v are the relativistic mass and velocity respectively, and h the Planck's constant. In a TEM, the electrons are accelerated at high voltage (100-1000 kV) to a velocity approaching the speed of light (0.6-0.9 c); they must therefore be considered as relativistic particles. The associated wavelength is five orders of magnitude smaller than the light wavelength (0.04-0.008 Å). A magnetic coil can focus an electron beam in the same way that a glass lens for light but the magnetic lens aberrations limit the convergence angle of the electron beam to 0.5° (instead of 70° for the glass lens used in optics), and increase the TEM resolution to the order of angstroms. This resolution enables material imaging at the atomic level.

2.3.2 Diffraction in TEM

In classical physics, the diffraction phenomenon is described as the apparent bending of waves around small obstacles and the spreading out of waves past small openings. In TEM, if we consider electron beam as a wave and atoms as small obstacles then a crystal material would work the same way as diffraction grating. In such a way, diffraction becomes the most important phenomenon in TEM. The reason for this importance is that information about the spacing of the planes in crystals and large amount of crystallographic information from space-group symmetry data right down to the dimensions of single unit cells can be obtained. At the most basic level, the interplanar spacings in different crystal structures are characteristic of that structure. The positions of the diffracted beams of electrons are determined by the size and shape of the unit cell and the intensities of the diffracted beams are governed by the distribution, number, and types of atoms in the specimen. The idea of using diffraction to probe the atomic structure of materials was credited to von Laue (1913) in Germany. Von Laue's crucial idea was that much shorter electromagnetic rays than light would cause diffraction or interference phenomena in a crystal.

Usually in TEM, an approach made by Bragg is used to describe diffraction. In this approach the path difference between electron waves reflected from the upper and lower planes in Figure 2.16 is (AB + BC). Thus, if the 'reflecting' hkl planes are spaced distance 'd' apart and the wave is incident and reflected at an angle θ_B, both AB and BC are equal to $d \sin \theta_B$ and the total path difference is $2d \sin \theta_B$. This equation is known as Bragg's law [2.27]:

$$n\lambda = 2d \sin \theta_B; \tag{2.10}$$

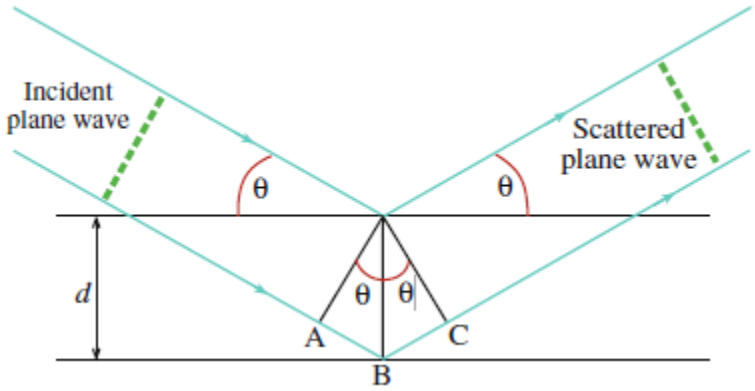

Fig. 2.16 Bragg's approach for calculating path difference between two planes [2.27]

2.3.4 Diffraction pattern

In previous paragraph diffraction from two parallel planes was explained. In real crystal we can count almost infinite number of planes and therefore the general picture looks different. Say we have many parallel planes each a distance *d* from its neighbors, as is shown in Figure 2.18. In the special case of Bragg diffraction, the scattering semiangle between the incident beam and the Bragg diffracted beam is twice the Bragg angle ($2\theta_B$).

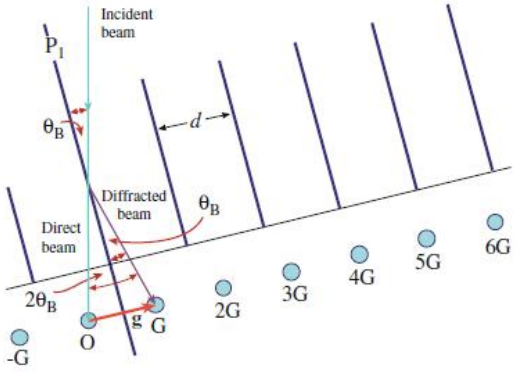

Fig. 2.18 Diffraction from a set of planes distance *d* apart [2.27]

We can see that in practice there will not just be one Bragg reflection but a series of reflections which are periodically spaced along a line; these are known as a systematic row of reflections, –G, 0, G, 2G, 3G, etc., with corresponding diffraction vectors, ***g, 0, g, 2g, 3g***, etc. ***g*** vector is also called diffraction vector and is defined as $\boldsymbol{g} = 1/d$, where *d* is the distance between the planes. This was a two dimensional example, but a real crystal has three dimensions and diffraction as not a row of dots anymore but a two dimensional pattern. An example of real diffraction pattern of Silicon is shown in figure 2.18.

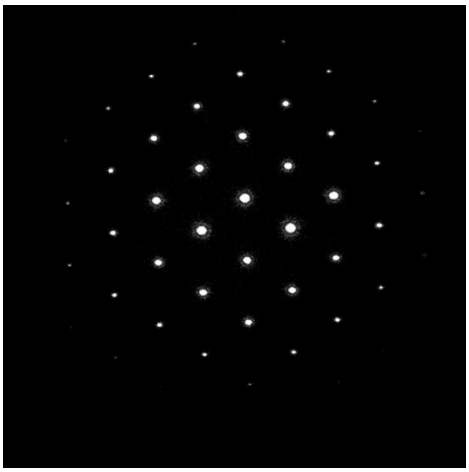

Fig. 2.18 Silicon diffraction pattern

2.3.5 EDS analysis

Energy-dispersive X-ray spectroscopy (EDS or EDX) is an analytical technique used for the elemental analysis of a sample.

First of all, a high-energy beam electron must penetrate through the outer conduction/valence bands and interact with the inner-shell (or core) electrons. If more than a critical amount of energy is transferred to an inner-shell electron, that electron is ejected; i.e., it escapes the attractive field of the nucleus, leaving a hole in the inner shell. The ionized atom can return almost to its lowest energy (ground state) by filling in the hole with an electron from an outer shell. This transition is accompanied by the emission of either an X-ray or an Auger electron. In both the X-ray and Auger cases, the energy of the emission is characteristic of the difference in energy between the two electron shells involved and this energy difference is unique to the atom. This means that X-ray photons emitted from an atom carries information about this atom and if collected by a detector it gives elemental data about elemental composition of the sample. An example of EDS spectrum is showed in figure 2.20.

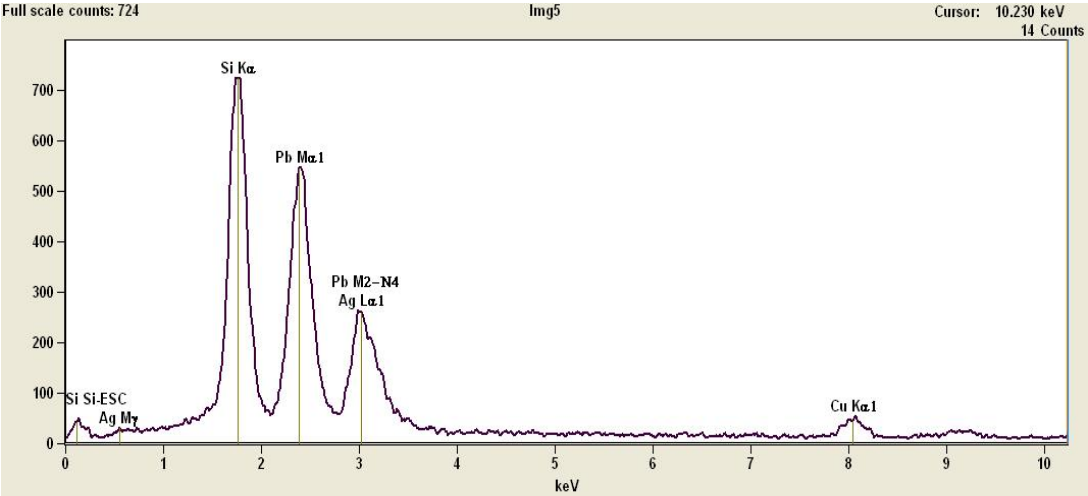

Fig. 2.20 EDS spectrum of one of the areas at Ag/Si interface

To produce spectra such as those in Figure 2.20, first a TEM image of the area you wish to analyze must be obtained. In TEM mode, you have to converge the beam to an appropriate size for analysis. It is recommended to tilt the sample slightly towards the EDS detector so that more X-rays can be detected.

In TEM, an intense beam of high-energy electrons bombards your specimen, which scatters many electrons. The specimen and any other part of the TEM that is hit by these electrons emit

both characteristic and Bremsstrahlung X-rays (which have energies up to that of the electron beam). Ideally, the spectrometer should only detect the X-rays from the beam-specimen interaction volume. However, as shown in Figure 2.21, it is not possible to prevent radiation from the stage and other areas of the specimen from entering the detector.

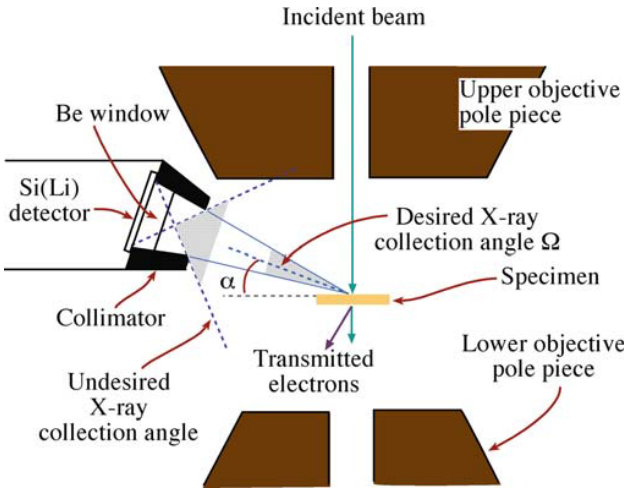

Fig. 2.21 Schematic diagram showing main parameters and parts of EDS system [2.27]

The detector collection angle (Ω) is the solid angle subtended at the analysis point on the specimen by the active area of the front face of the detector. The collection angle is shown in Figure 2.21 and is defined as:

$$\Omega = \frac{A \cos \delta}{S^2}; \qquad (2.11)$$

where A is the active area of the detector, S is the distance from the analysis point to the detector, and δ is the angle between the normal to the detector and a line from the detector to the specimen. So it is beneficial to tilt the sample towards the detector so $\delta = 0$, then $\Omega = \frac{A}{S^2}$. It is clear that to maximize Ω the detector should be placed as close to the specimen as possible. Count rate (photons detected per time period) is one of the most important parameters of EDS analysis and largely depends on collection angle.

3. Experimental

In this chapter methods and experimental procedure will be discussed. Firstly, instruments used for characterization and microscopy will be named with brief explanation of their working principles. Secondly, the procedure of experiment will be described. All steps will be introduced in consistent order with brief description of main parameters used and important notes. Two types of solar cells, semisquare multicrystalline (mc-Si) and Czochralski type circular monocrystalline (c-Si), were used in the project so all steps of procedure will be separated into two parts: one dedicated for mc-Si, another - for c-Si.

3.1 Methods

3.1.1 Solar simulator

Finished solar cells were characterized using the solar simulator. A solar simulator is a device that provides artificial radiation of sunlight. A solar cell is illuminated using a special lamp which serves as a source of AM1.5 solar spectrum sunlight. A varying voltage bias is applied across the cell contacts, and the generated current is continuously measured. By this procedure current-voltage (I-V) curves are obtained. From I-V curves further data like open circuit voltage, short circuit current, fill factor, efficiency etc. can be calculated.

3.2.2 Series resistance mapping

IV curves measurements give sufficient data about the quality and main parameters of the solar cell. This general data gives information about the average quality over whole area of solar cell, while microscopy experiments require samples from specific regions. The quality of the cell is determined by the quality of the contacts and the best measurement for it is series resistance (R_S). This critical electrical parameter of solar cells can vary noticeably across the cell area. A series resistance mapping by using photoluminescence imaging (PL-R_S technique) is a fast and robust technique for spatially resolved measurements of the series resistance. The operation principle of this technique will be explained in this paragraph.

In theoretical model the solar cell is described as a two dimensional network of individual nodes. An equivalent circuit of a node is shown in Fig 3.1.

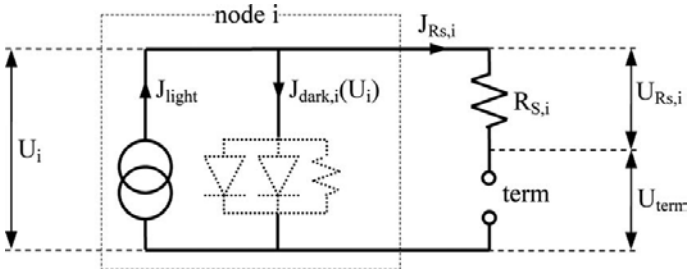

Fig 3.1 Equivalent circuit of one node at position *i*, which corresponds to image pixel *i* [3.1]

Each node *i* contains a current source J_{light}, an unknown dark current density $J_{\text{dark},i}(U_i)$ and a series resistance R_S. The characteristics of $J_{\text{dark},i}(U_i)$ can be modeled by the same two-diode model, which includes a shunt resistance parallel to the diodes. The effective series resistance of node *i*, $R_{S,i}$, is the sum of all transport resistances in the current path from one terminal to the other terminal of that node. It also includes light generated effects of current generation and recombination of other nodes in the current path.

In this technique series resistance is determined from two images at different luminescence intensities but under different operating conditions. It can be shown that series resistance of each node can be expressed as following:

$$R_{S,i} = \frac{\Delta U_{R_{S,i}}}{\Delta J_{R_{S,i}}} = \frac{\Delta U_i - \Delta U_{term}}{\Delta J_{light} - \Delta J_{dark,i}}, \tag{3.1}$$

where $\Delta U_{R_{S,i}}$ is the difference in voltages across the series resistance between the two operating points and $\Delta J_{R_{S,i}}$ is the difference in current densities. These can be expressed by the differences in local diode voltage ΔU_i, the difference in terminal voltage ΔU_{term}, the difference in light generated current density ΔJ_{light}, and the difference in dark current density $\Delta J_{dark,i}$. Fig. 3.2 shows these measurements on IV curve where solar cell is operated at two different operating points.

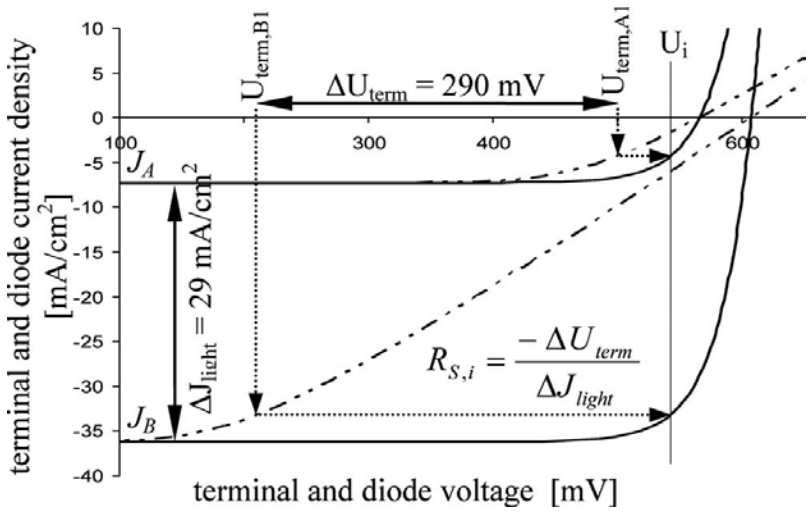

Fig. 3.2 *I-V* curves of one node *i* at two illumination intensities with $J_{\text{light,A1}}$=7 mA/cm^2 and $J_{\text{light,B1}}$=36 mA/cm^2. Solid curves are the *I-V* characteristics without series resistance (i.e., current density as a function of the diode voltage). Broken curves include the effect of series resistance of 10 Ωcm^2. The solid vertical line represents the diode voltage U_i, corresponding to terminal voltages $U_{\text{term,A1}}$ and $U_{\text{term,B1}}$ [3.1]

As stated in [3.1] measuring identical offset corrected luminescence signals at two different operating conditions is equivalent to identical diode voltages U_i. This means that in Eq. (3.1) term ΔU_i becomes equal to zero. What is more, identical diode voltages give identical dark current densities and term $\Delta J_{dark,i}$ in Eq. (3.1) is equal to zero as well. Eq. (3.1) simplifies to

$$R_{S,i} = \frac{-\Delta U_{term}}{\Delta J_{light}}, \tag{3.2}$$

where $-\Delta U_{term}$ is voltage difference between the terminals and ΔJ_{light} is the difference in short circuit current densities. Both can be easily measured between the terminals under the assumption that the short circuit current density is constant across the cell.

The above correlation between luminescence signal and local diode voltage can be made since the luminescence signal is an exponential function of the local diode voltage U_i [3.2],

$$I_{camera,i} = C_i \exp\left(\frac{eU_i}{kT}\right) + C_{offset,i}, \tag{3.3}$$

where *e* is the electron charge, *k* the Boltzmann constant, and *T* the junction temperature.

C_i is a voltage dependent calibration constant, which accounts for locally varying optical properties and variations in the luminescence signal of the cell due to variations in the local diffusion length of minority carriers [3.3]. $C_{\text{offset},i}$ is a junction voltage independent offset

constant of the luminescence signal. It is caused by radiative recombination of diffusion-limited carriers and can be measured experimentally for a given illumination intensity and for each pixel by taking a luminescence image at short circuit conditions (when first term in Eq. (3.3) is negligible). In practice all luminescence images are corrected to eliminate the offset $C_{\text{offset},i}$.

In comparison with other techniques luminescence series resistance imaging has several advantages. It is demonstrated experimentally that PL imaging is sensitive to series resistance effects occurring on both the front and the rear surface in contrast to Corescan, which only measures front surface effects [3.4]. Figure 3.3 shows the comparison of the series resistance of a screen printed monocrystalline silicon solar cell determined using the quantitative PL-R_s method with a Corescan measurement taken on the same cell.

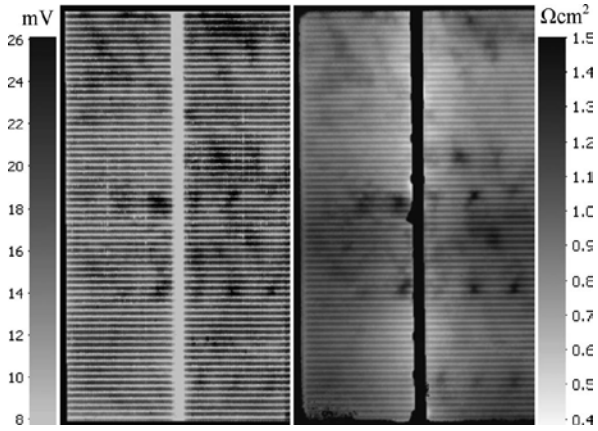

Fig. 3.3 Left: Corescan image showing the voltage drop toward the terminal. Right: R_S-image of the same area. Same high series resistance areas are observed in both images [3.4]

The PL image shows the series resistance in Ωcm^2, whereas the Corescan presents the local voltage drop between emitter and front grid. The PL-R_s method is advantageous as it provides better spatial resolution with significantly shorter data acquisition time. The data acquisition time required for the PL-R_s method is thus compatible with in-line process monitoring. Another important consideration that is crucial for in-line applications is that the PL-R_s technique is non-destructive.

In conclusion, this method is a very useful tool for this project and allows acquiring fast and good quality spatially resolved series resistance maps of silicon solar cells.

3.2.3 Transmission electron microscope

TEMs are capable of imaging at a significantly higher resolution than light microscopes, due to the small de Broglie wavelength of electrons. This enables examination of extremely fine detail—even as small as a single column of atoms, which is tens of thousands times smaller than the smallest resolvable object in a light microscope.

Depending on the settings of the microscope, different microscopy modes are possible. Selected area diffraction (SAD), energy dispersive X-ray spectroscopy (EDS) and imaging modes being the only ones used in this work. In Figure 3.4 a simplified ray diagram is illustrated.

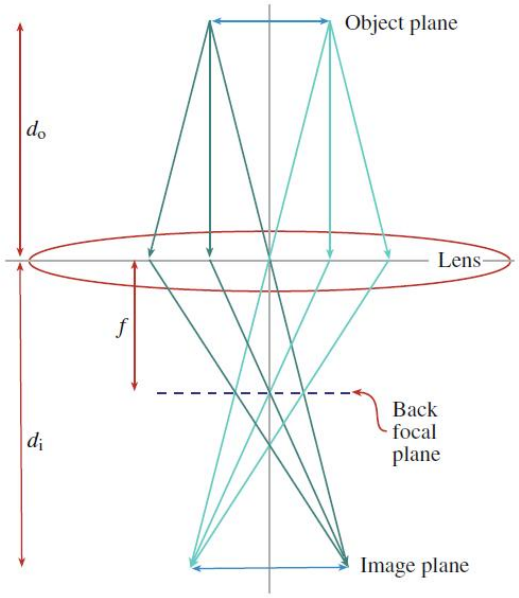

Fig. 3.4 Simplified TEM ray diagram [3.5]

In Figure 3.4, all rays from a point in the object are brought back to a point in the image and all parallel rays (whether parallel to the optic axis or not) are brought to a focus in a plane at a position depending on their angle to the axis. On-axis parallel rays are focused on axis and off-axis parallel rays are focused off axis. This is a most important property, since it allows the lens to create diffraction patterns (DP) in the focal plane.

Diffraction mode: to see the DP the imaging-system lenses have to be adjusted so that the back focal plane of the objective lens acts as the object plane for the intermediate lens. Then the DP is projected onto the viewing screen/CCD as shown on the left side of Figure 3.5.

Image mode: to see an image, readjusting the intermediate lens is needed so that its object plane is the image plane of the objective lens. Then an image is projected onto the viewing screen/CCD, as shown on the right side of Figure 3.5 [3.5].

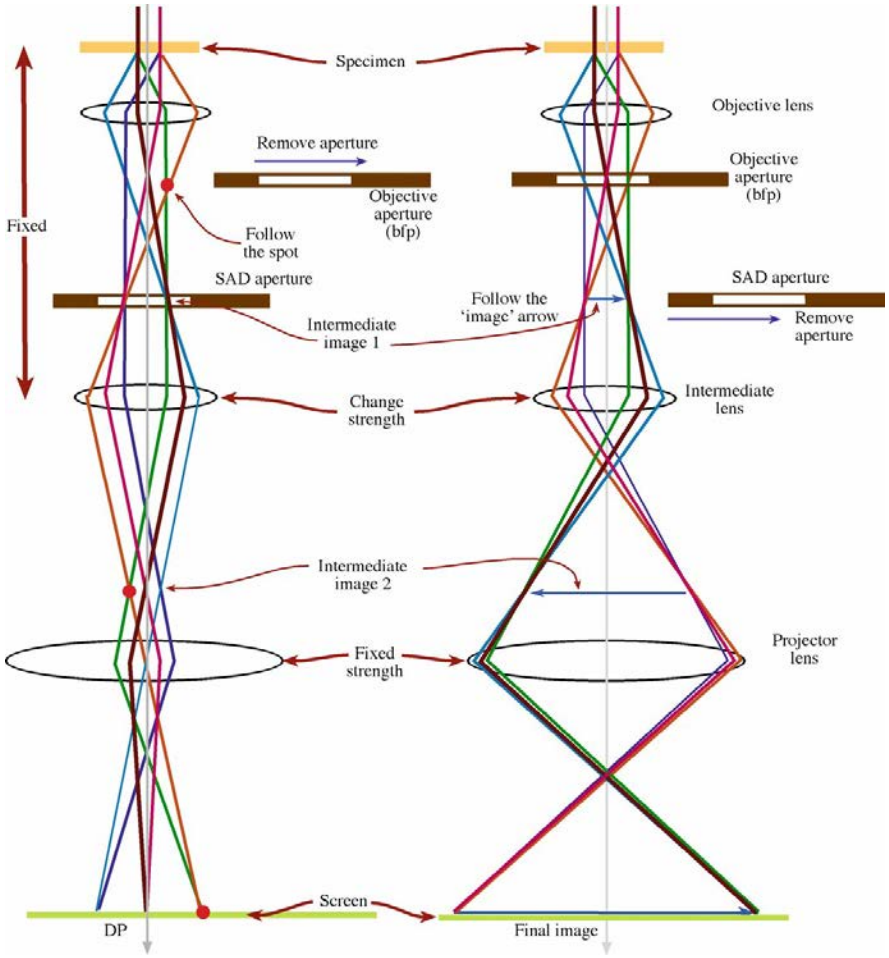

Fig. 3.5 The two basic operations of the TEM imaging system: (left) diffraction mode and (right) image mode [3.5]

EDS analysis: to get X-ray spectrum, TEM was set to imaging mode. Sample was tilted about 10˚ towards detector to increase collection of X-rays and improve the quality of the spectrum. Electron beam was converged to a maximally low spot size on a region of interest. Some extremely small features of size below 50 nm could not be analyzed with high accuracy as a lot of noise signal were collected from surroundings.

3.2 Experimental procedure

3.2.1 The cells

At first, an experiment with multicrystalline Si (mc-Si) solar cells was performed. Multicrystalline Si cells are composed of many smaller Si crystals randomly oriented in the cell. Multiple orientations of the crystals have influence on microscopic and macroscopic parameters and features of the contacts. In addition, monocrystalline cells were investigated to supplement the study.

In this project two types of cells were used: semi-square multicrystalline and circular Czochralski type monocrystalline cells. All cells were manufactured up to the step of metallization and were provided by Institute for Energy Technologies (IFE). The mc-Si cells were textured, square shaped (125mm x 125mm), about 200 μm in thickness with rounded corners. The c-Si cells were double side polished circular wafers, 100 mm in diameter, 275-325 μm in thickness, with surface oriented along (100) direction. Both types of cells had SiN anti-reflection coating (ARC).

c-Si cells because of their circular shape were not convenient to use for metallization as there was no screen for printing contacts on such kind of cells. Hence, four smaller square shaped cells (25mm x 25mm) were cut from each circular cell using laser.

3.2.2 Screen-printing

17 mc-Si and 24 c-Si cells were prepared for screen-printing. All the cells were printed using the same pastes: Al52-140 paste for backside and NS33-512 paste for front side (characteristics can be found in [4.1] and [4.2] respectively). Printing parameters were loaded from special files where optimized parameters were saved for specific type of cell and screen. Snap-off distance was set to an optimal value of 1 mm.

The screen-printing process was performed as follows:

1. Printing full back side Al contacts.
2. Drying for several minutes at 300˚C.
3. Printing front side Ag contacts.
4. Drying for several minutes at 300˚C.

A screen-printing machine with automatic alignment function was used, which helped to perform this step in a fast and easy way.

3.2.3 Firing

Until the firing step no differences in manufacturing processes were introduced (except differences between mc-Si and c-Si cells). This meant that all mc-Si cells were equivalent (had the same properties) and all c-Si were equivalent.

During the firing step the peak firing temperature (PFT) had been varied. After firing the cells were expected to have different electronic properties. The goal of this step was to get highest quality optimally fired cells and lower quality under fired and over fired cells.

mc-Si cells

Multicrystalline cells were divided into eight groups by two for different firing profiles. One extra cell was fired at 940°C peak temperature. Firing furnace had four sections with distinct temperatures, so firing profile could be described by defining the temperatures of each of the sections. For example in 1st section PFT was set at 780 °C, in 2nd section at 830 °C, in 3rd section at 875 °C and in 4th at 920 °C then firing profile could be described as "780°C/830°C/875°C/920°C". The firing time depended on the speed of the belt. In this experiment an optimized belt speed of 400 cm per minute was used, giving firing time of approximately one minute. Information about the firing setup for the mc-Si cells is provided in table 4.1.

Cell place in the holder	Temperature profile	Belt speed
1, 2	780 °C/800 °C/820 °C/840 °C	@400cm/min
3, 4	780 °C/805 °C/830 °C/860 °C	
5, 6	780 °C/810 °C/845 °C/880 °C	
7, 8	780 °C/820 °C/860 °C/900 °C	
9, 10	780 °C/830 °C/875 °C/920 °C	
11, 12, 13	780 °C/835 °C/885 °C/940 °C	
14, 15	780 °C/840 °C/900 °C/960 °C	
16, 17	780 °C/850 °C/915 °C/980 °C	

Table 4.1 Firing parameters for mc-Si solar cells.

c-Si cells

The c-Si solar cells were divided into nine groups by 3. Each set of 3 cells were held into one box, boxes have been indexed from 1 to 9. At this point it is necessary to come ahead of the further events and say that after firing c-Si cells seemed to have smaller efficiencies than expected. It was found out that it was caused by the fact that during firing the temperature in the middle part of the belt was about 40 degrees lower than the sides. These differences were clearly seen on the mc-Si solar cells which were large in area. The c-Si cells were small and were placed in low temperature zone, thus their average efficiency was lower. This means that cells fired at temperatures set to 860°C were fired actually at about 820°C. Cells fired at lower peak temperatures (840°C and 860°C) had their back side contact still wet. The optimization was achieved for the cells fired at 960°C.

Box	Temperature profile	Belt speed
1	780 °C/810 °C/840 °C/860 °C	
2	780 °C/815 °C/850 °C/880 °C	
3	780 °C/820 °C/860 °C/900 °C	
4	780 °C/825 °C/870 °C/920 °C	
5	780 °C/830 °C/880 °C/940 °C	@400cm/min
6	780 °C/840 °C/900 °C/960 °C	
7	780 °C/850 °C/915 °C/980 °C	
8	780 °C/855 °C/930 °C/1000 °C	
9	780 °C/860 °C/940 °C/1020 °C	

Table 4.2 Firing properties for c-Si solar cells.

3.2.4 Edge isolation

The edge isolation process was used to remove the phosphorous diffusion around the edge of the cell so that the front emitter is electrically isolated from the cell rear and shunt resistance is maximized. In this experiment edge isolation was performed using laser.

The c-Si cells were cut by laser from CZ wafer without any pollution on the edges and no additional edge isolation was required.

After edge isolation cells were ready for characterization and are shown in figure 3.6

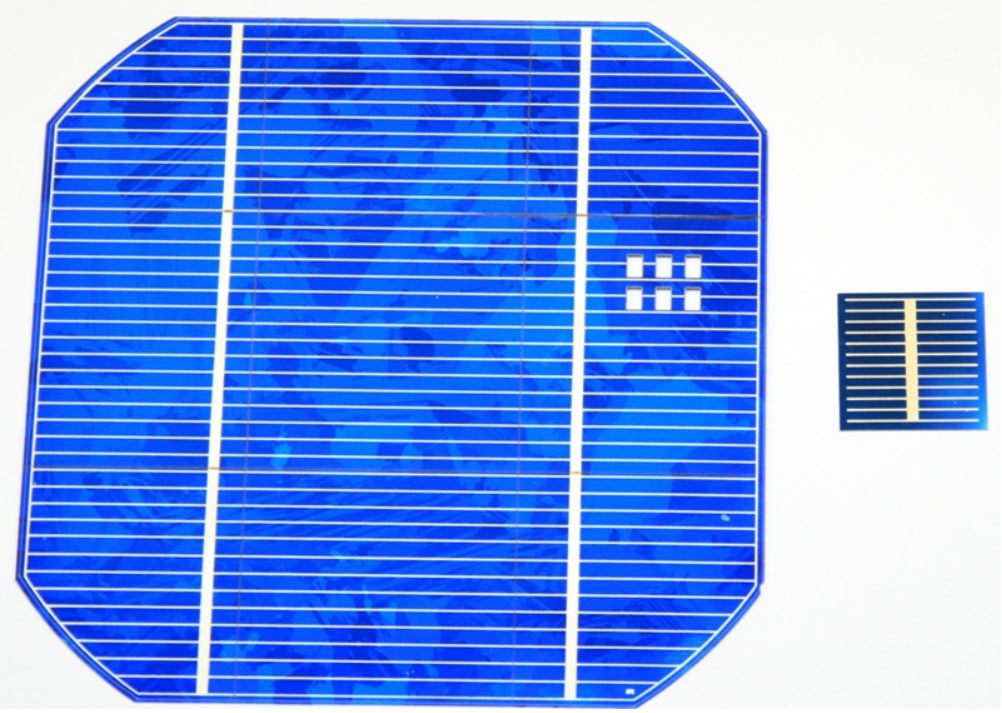

Fig. 3.6 Picture of semi-square mc-Si cell and square shaped c-Si cell cut from CZ type cell. The six holes is the mc-Si were left after laser-cutting samples for TEM investigation

3.2.5 Performance characterization

The solar cells needed to be checked if they were manufactured with satisfied quality and did not have any significant defects. As written above, cells were fired at different temperatures and efficiency optimization was expected at some temperature. Away from this temperature efficiencies together with fill factors were supposed to deteriorate. In order to check this, current-voltage (I-V) measurements were performed for all solar cells using solar simulator. Illumination equivalent to standard AM1.5 solar spectrum was used for measurements under room temperature.

3.2.6 Series resistance mapping

A PL/EL mapping machine LIS-R1 was used to get spatially resolved measurements of the effective series resistance of silicon solar cells from luminescence images. Separate calibration had to be done for mc-Si and c-Si cells because of difference in size and electrical properties.

3.2.7 Sample preparation for TEM

Sample preparation was the hardest and most time consuming task in the whole project. Skills of precision, particularity, determination and attentiveness to every detail were necessary to get a successful sample. Even after mastering sample preparation about 30% of the samples were successful.

Sample preparation started by cutting small rectangles (~3mm x 4mm) from area of interest. Rectangles were cut so that finger line is perpendicular to one of the sides (preferably the longer one) (Figure 3.7).

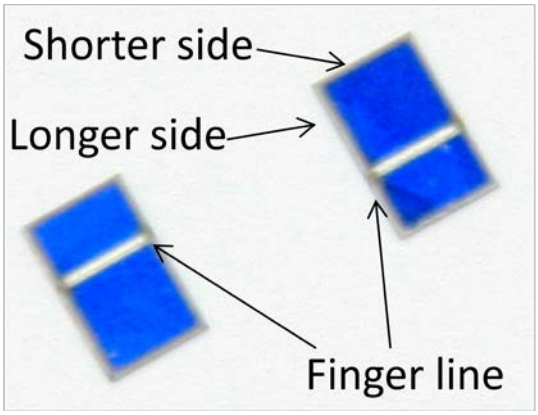

Fig. 3.7 Example of two rectangles cut from solar cell with finger line perpendicular to longer side of the sample

Two such rectangles were then glued facing each other with two extra layers of silicon wafer (no contact) on each side to buffer the sample. This multi layered sample was then glued on a stub and mechanically grinded from top and bottom to get as thin and smooth specimen as possible (~20 μm is a satisfactory thickness). This very thin cross-sectional sample is then glued on a copper grid which serves as a support for the TEM sample. Copper grid is 3mm in diameter and is made to fit into TEM sample holder. Sample with copper grid were finally polished using GATAN precision ion polishing system (PIPS Model 691) until it is electron transparent and ready for TEM imaging. In PIPS machine sample is mounted into special holder and set to rotate around the axis perpendicular to the surface of the sample. Two ion guns are aligned so that they bombard the ions exactly at the point around which sample is rotating. This step was tricky because ion beams needed to be targeted exactly at the interface of silicon wafer and silver

contact which is 100-200 μm long. Usually small tilt of the sample and not very accurate ion beam alignment caused target shifting. Another problem was different polishing rates of silver and silicon. If beams were targeted on cross section, the silver got removed very fast and sample was useless for further investigation. A solution was to mount the sample so that rotation axis is not exactly on the cross-section or Ag/Si interface but slightly further on Si wafer (fig. 3.8).

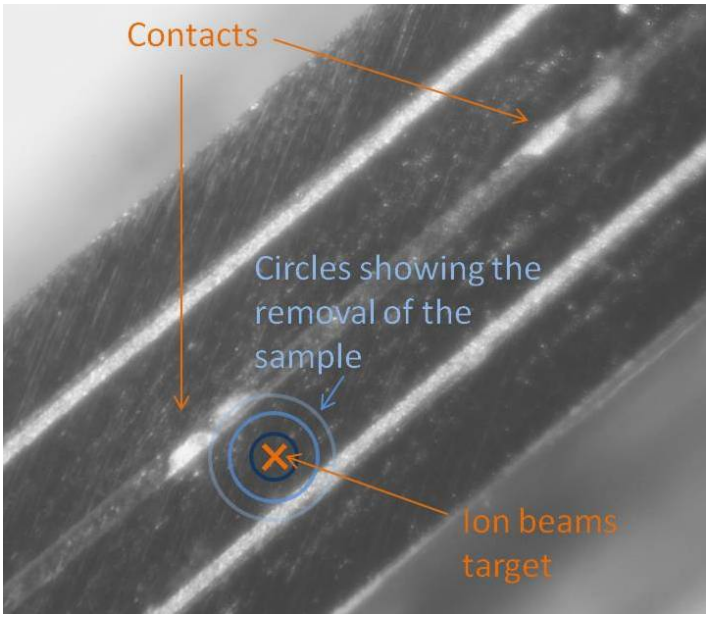

Fig. 3.8 Example of correct targeting of ion beams

The following properties were used for ion milling:

Energy: 4.5 keV at the beginning, 4 keV when finishing the sample.

Top angle: 7 degrees.

Bottom angle: 6 degrees.

Rotation: 3 rpm.

3.2.8 Transmission electron microscopy

A JEOL 2000FX transmission electron microscope with LaB_6 electron gun and equipped with EDS system was used. Double tilt sample holder was chosen for operation. TEM was operated at an acceleration voltage of 200 kV. To calculate *d* values from diffraction patterns a camera length of 66 cm was used. All images were taken on photographic plates.

4. Results and discussion

In this chapter results will be presented and discussed. First, correlation between solar cell performance and peak firing temperature will be analyzed. Second, spatially resolved series resistance images will be discussed. The chapter will be finished with TEM investigations which include images, diffraction patterns and EDS spectra. In this chapter different sections are again divided into two parts: one about mc-Si and another about c-Si solar cells.

4.1 Solar cell efficiency

The best parameter to compare solar cell performance is efficiency. As stated above, in this experiment firing temperature was varied in order to get high performance optimally fired cells and lower performance under fired and over fired cells. The goal was to achieve efficiency optimization at some specific temperature.

As mentioned before, the performance of the solar cells was investigated using solar simulator. The IV curves from each of the cells were simulated and the main properties were extracted.

4.1.1 Multicrystalline-Si cells

The correlation of efficiency with firing temperature of mc-Si solar cells is shown in figure 4.1.

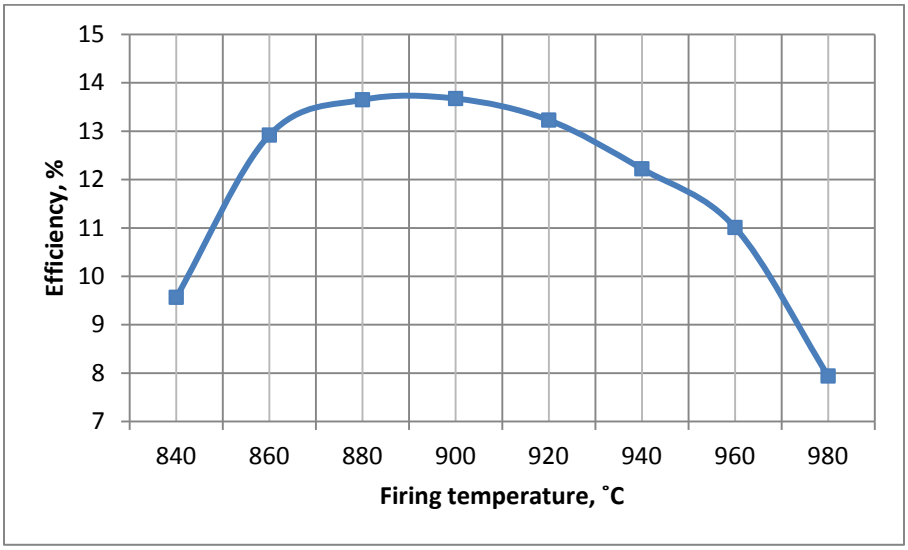

Fig. 4.1 Efficiency dependence on firing temperature in mc-Si solar cells

In this graph it can be seen that optimization was achieved for cells fired at 880˚C and 900˚C. An abrupt fall of efficiency occurs at lower temperatures. Efficiency drops as well when firing

temperature increases further from optimal. At first the slope is gentle but drops rapidly at 980˚C.

4.1.2 Crystalline-Si cells

The correlation of efficiency with firing temperature of c-Si solar cells is shown in figure 4.2.

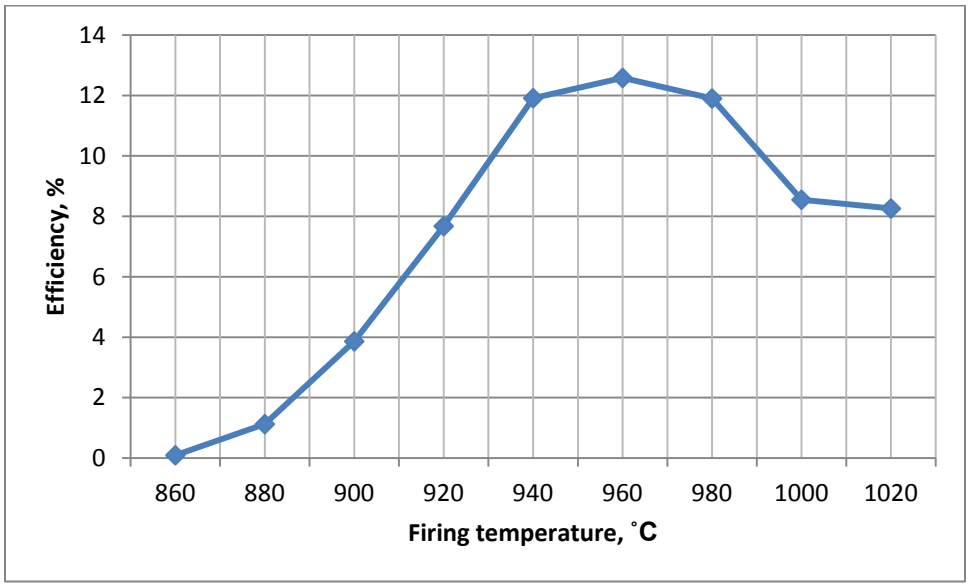

Fig. 4.2 Efficiency dependence on peak firing temperature on c-Si solar cells

After firing some the crystalline Si solar cells optimization was achieved at the temperature of 960˚C. However, this graph is slightly different in shape and temperature value at which optimization was reached when compared to mc-Si cells. The reasons were briefly covered in the preceding chapter but will be explained in more detail here.

4.1.3 Problems with furnace

The metallization furnace used in this experiment had four heating sections. Each of these sections had three heating parts: one heating the cells from the bottom (under the belt) and two from the sides. Therefore, during firing heat came from underneath the cell and from the sides as painted in figure 4.3.

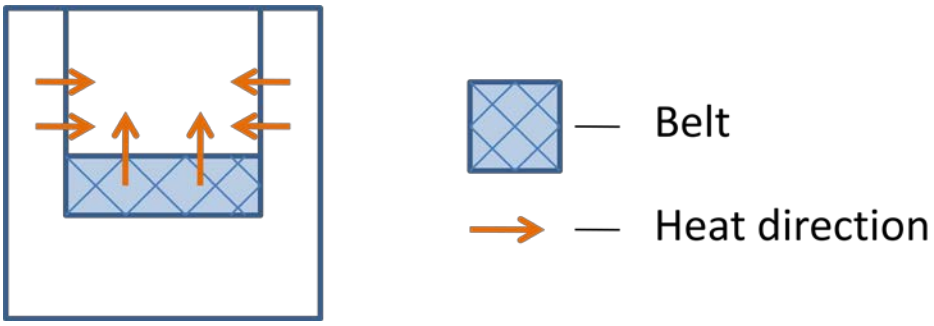

Fig. 4.3 A schematic view of firing furnace from the front

Due to defective calibration, temperature was much higher at the sides of the belt, while the middle part was slightly cooler. If, for example, peak firing temperature was set to 960˚C then optimal temperature for c-Si solar cells (which were placed in the middle part of the belt) was reached. However, temperature on the sides was higher and because mc-Si solar cells were much larger than c-Si, their sides suffered from over firing. If peak temperature was set to 900˚C which was optimal for mc-Si cells then the quality of c-Si cells suffer from under firing. Consequently, two problems occurred:

- There always were over firing on the sides or under firing in the middle, thus maximum efficiency could not be reached on mc-Si solar cells.
- Non-uniform firing pattern caused differences in series resistance on mc-Si solar cells.

First problem was not very relevant in this project as the goal was not to reach the highest possible efficiency, but to get optimally fired cell together with under and over fired cells. The second problem had more importance but was easily solved by using spatially resolved series resistance mapping instrument as will be showed later.

4.2 Fill factor

As stated in Chapter 2, fill factor is a parameter which reflects both parasitic resistances. Therefore, it not only shows the quality of solar cell but is a good parameter for determining the quality of the contacts. In addition, it is possible to determine what kind of parasitic resistance is dominating by checking the shape of I-V curves.

4.2.1 Multicrystalline-Si cells

In figure 4.4 the correlation of fill factor with peak firing temperature of mc-Si solar cells is shown.

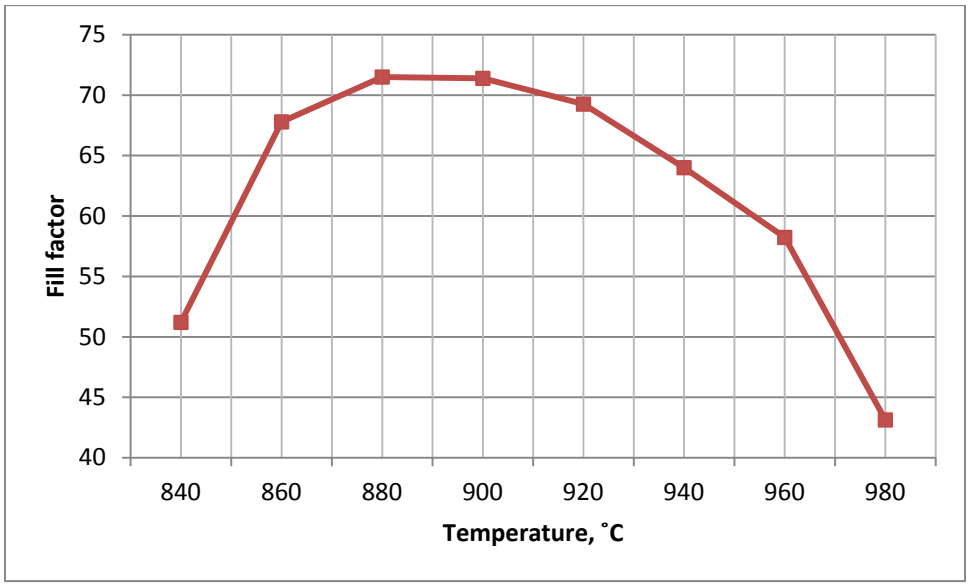

Fig. 4.4 Fill factor dependence on peak firing temperature on mc-Si solar cells

The shape of the curve is similar to that of efficiency and this shows that there were no major differences between the cells only these related with metallization. For this reason all performance variations can be explained as effects of series and shunt resistances.

First of all, a steep fall of FF occurs at lower firing temperatures of 840˚C and 860˚C. When firing temperature increases further from optimal - efficiency drops as well. To explain the reasons for these drops the IV curves are included below.

In figure 4.5 the I-V curves of under fired and over fired cells are compared with optimally fired cells.

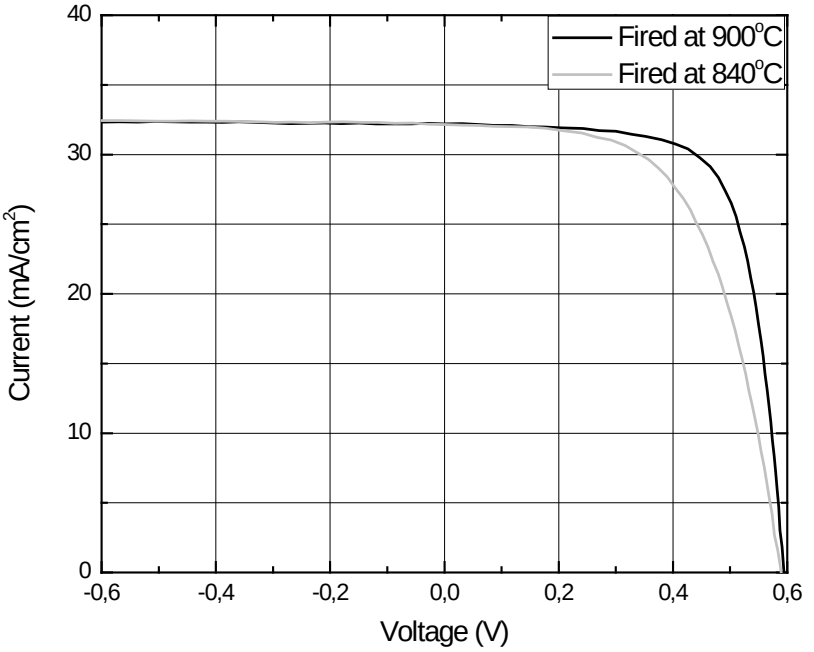

a)

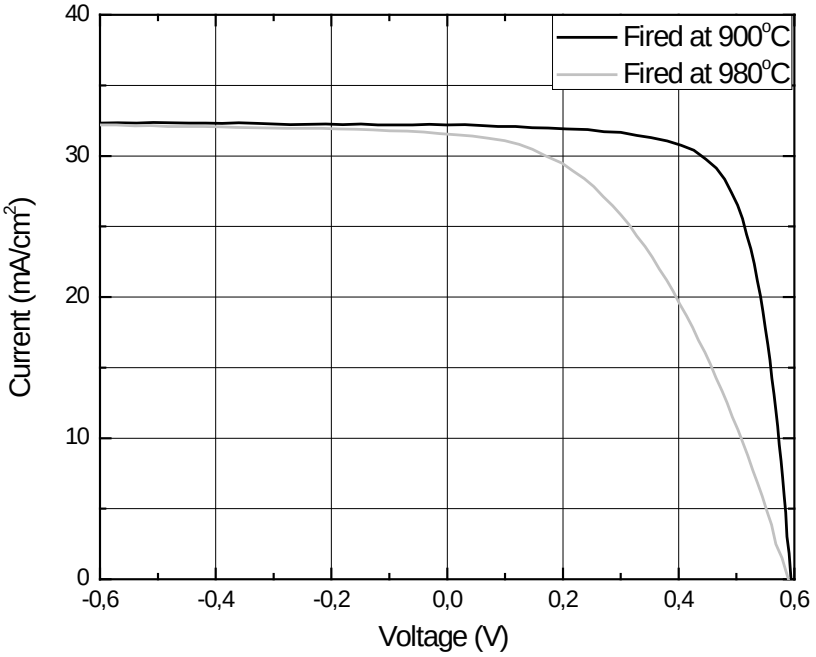

b)

Fig. 4.5 An I-V curve comparison of mc-Si a) under fired and optimally fired cell and b) of over fired and optimally fired cell

As explained in sub-chapter 2.1.7, series resistance reduces FF and changes the shape of I-V curve as shown in figure 2.6. When series resistance increases to excessively large values it starts to reduce short circuit current. The graph 4.5a is similar in shape to IV curve in figure 2.6a suggesting that FF of cells fired at lower than optimal temperature is reduced because of series resistance. A similar case is with over fired cells. High series resistance causes a slightly inclined slope of I-V curve of over fired cell. This curve shows a small inclination at negative values as well. This is a confirmation of shunt resistance.

Although only I-V curves of the cells fired at the lowest and the highest temperatures are depicted in figure 4.5, I-V curves of cells fired at mediate temperatures fall nicely into the trend and support the previous statements.

4.2.1 Crystalline-Si cells

The correlation of FF with peak firing temperature of c-Si solar cells is shown in figure 4.6.

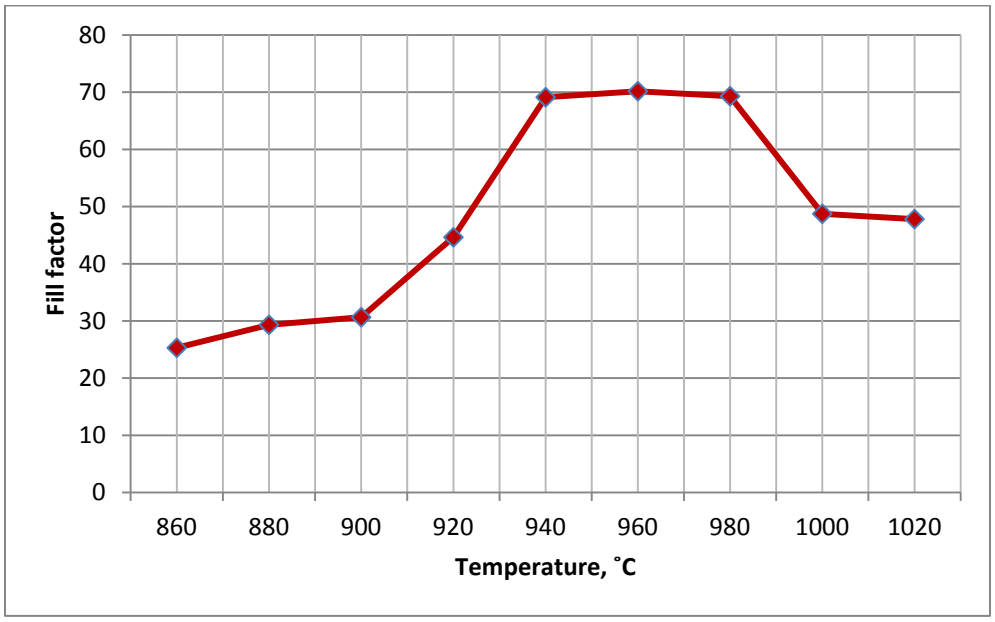

Fig. 4.6 Fill factor dependence on peak firing temperature on c-Si solar cells

Similarly to mc-Si solar cells, the FF dependence on firing temperature has a similar shape to efficiency dependence. Cells fired at temperatures 940˚C, 960˚C and 980˚C were very close in quality. Cells fired at 960˚C were the most efficient and this temperature is considered to be optimal. Under firing and over firing causes a drop of FF. To find out the reasons for these drops the comparison of I-V curves is included in figure 4.7.

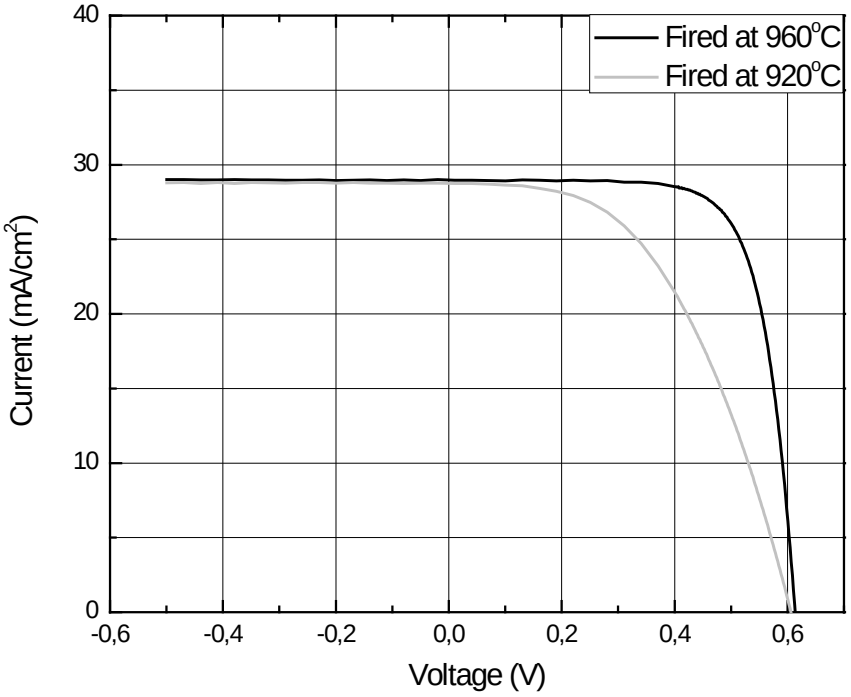

a)

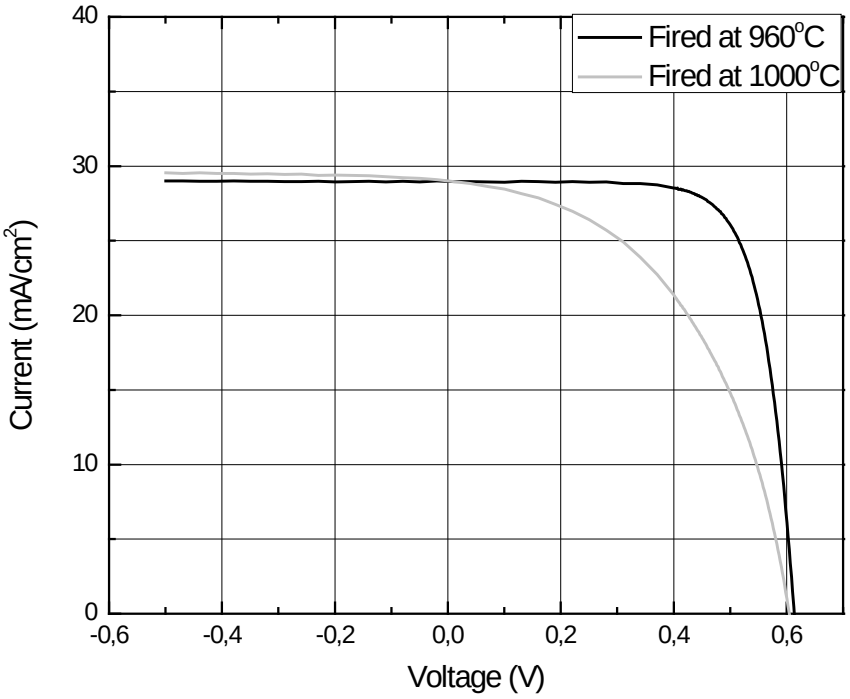

b)

Fig 4.7 An I-V curve comparison of c-Si a) under fired and optimally fired cells and b) of over fired and optimally fired cells

Graph in figure 4.7a shows a strong effect of series resistance on under fired cell when compared with optimally fired cell. No shunting is observed as the graph is perfectly flat at horizontal part of I-V curve. In over fired cell the reason for FF reduction are both parasitic resistances. An incline of small degree at negative values proves the existence of shunt resistance. The slope of the vertical part of I-V curve implies that series resistance has a large influence on reduction of fill factor.

4.3 Series resistance

The goal of this project was to investigate solar cells fired at different temperatures and determine, by using electron microscopy, why cells fired at certain temperatures are better than others. Solar simulator gave the main parameters of the cells but these parameters were average over the whole area of the cell. Due to the spatial variation of series resistance across the area of the cell, samples could not be cut from anywhere. Spatially resolved series resistance maps were needed in order to correctly choose the area of interest from where samples could be cut.

4.3.1 Multicrystalline-Si cells

Series resistance maps were obtained for mc-Si solar cells and are shown in figure 4.8 with firing temperatures indicated at right bottom corner of the pictures.

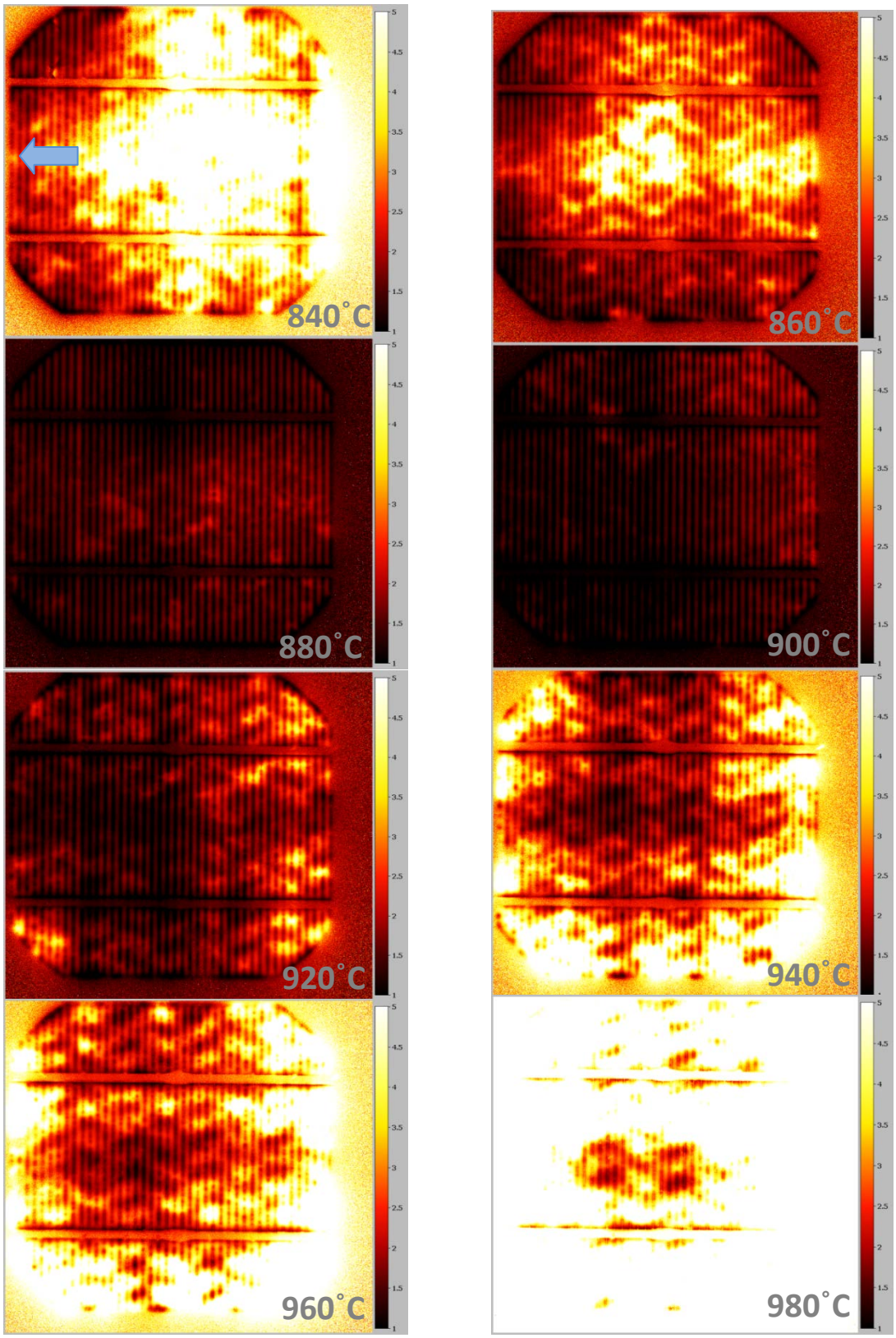

Fig. 4.8 Spatially resolved series resistance maps of mc-Si solar cells fired at different temperatures

The scale is the same for all pictures in order to reflect the differences between the cells. It varies from 1 Ωcm^2 (darker areas) to 5 Ωcm^2 (brighter areas). It is important to say that all cells were positioned on the belt of the firing furnace in the same way and the moving direction of the belt is indicated with the arrow on the first picture and is the same for all cells. As mentioned above the temperature in the firing furnace is higher on the sides and lower in the middle part. The wavy pattern of higher and lower series resistance is an imprint of metallic belt which works as a different medium for heat transport.

These eight pictures could be grouped into three groups: under fired (840˚C and 860˚C); optimally fired (880˚C and 900˚C) and over fired (920˚C, 940˚C, 960˚C and 980˚C). Cells from the first group have higher series resistance in the middle part and fairly low resistance on the sides. Because sides are almost optimally fired, the middle part must, therefore, be under fired due to the lower temperature in that part. Optimally fired cells possess series resistance maps which are uniform and with low average value of series resistance. When firing temperatures exceed 900˚C, series resistance gradually increases for higher temperatures. Over firing occurs on the sides of the cells while the middle part remains more efficient because of lower temperature, hence lower series resistance.

As a result, these maps help to pick the area of interest when considering TEM sample preparation. For example, if under fired cell is to be investigated, a sample from under fired part must be chosen. Without these maps one could take a sample from the side of the cell where contacts are almost optimally fired. In such a case, TEM investigation would give distorted results which would not reflect the real picture. In addition, series resistance mapping revealed the problem of firing furnace. It would not be possible to detect that problem from any other parameters, I-V curves or TEM investigations.

4.3.2 Crystalline-Si cells

Series resistance maps were obtained for c-Si solar cells and are shown in figure 4.9 with firing temperatures indicated below the pictures.

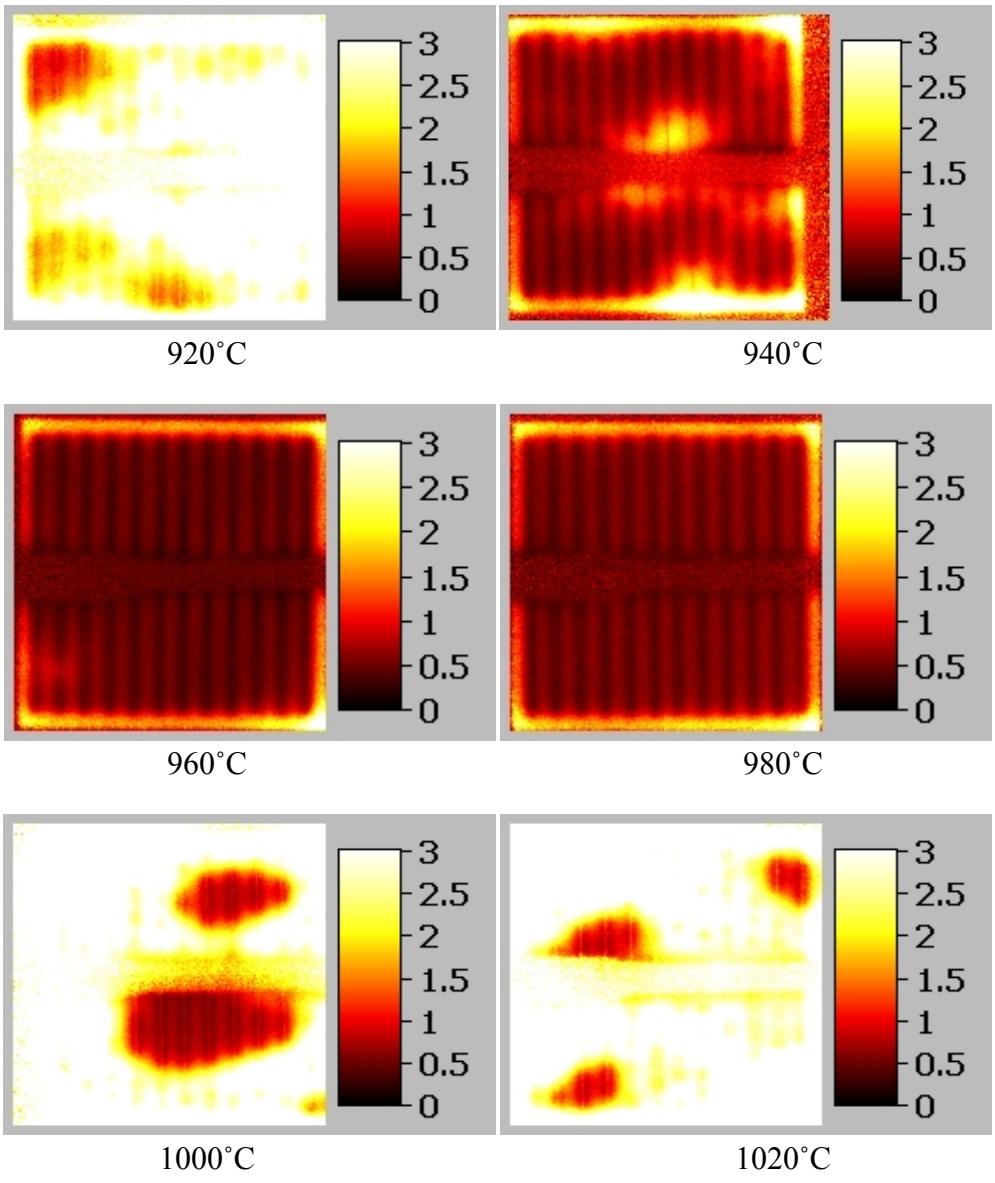

Fig. 4.8 Spatially resolved series resistance maps of c-Si solar cells fired at different temperatures

The results of c-Si solar cells are similar to these of mc-Si and could be explained in the same way. The difference between series resistance in the middle part and the sides could still be clearly seen, even though, the cells were much smaller and firing patterns were much more uniform.

4.4 TEM imaging and EDS

Samples for electron microscopy were made from under fired (UF), optimally fired (OPF) and over fired (OF) cells. From the batch of mc-Si solar cells, cell fired at 840˚C was chosen as under fired, cell fired at 900˚C was chosen as optimally fired and 980˚C was picked as over fired cell. From c-Si cells batch, cells fired at 920˚C, 960˚C and 1020˚C were picked as UF, OPF and OF cells respectively. If the cell was under fired, the material for sample making was cut from area which was most under fired (highest series resistance) according to the series resistance maps. Accordingly, samples of OF cell were taken from most over fired area. Circled areas on some of the samples indicate where EDS spot analysis was done. The texts in the circles correspond to the title of the spectra. In all EDS spectra some signal of copper was detected because during ion milling some copper was sputtered from the copper ring. The results will be discussed separately for the multicrystalline and the monocrystalline solar cells.

4.4.1 Multicrystalline-Si cells

4.4.1.1 Images of UF cell are shown in figure 4.9.

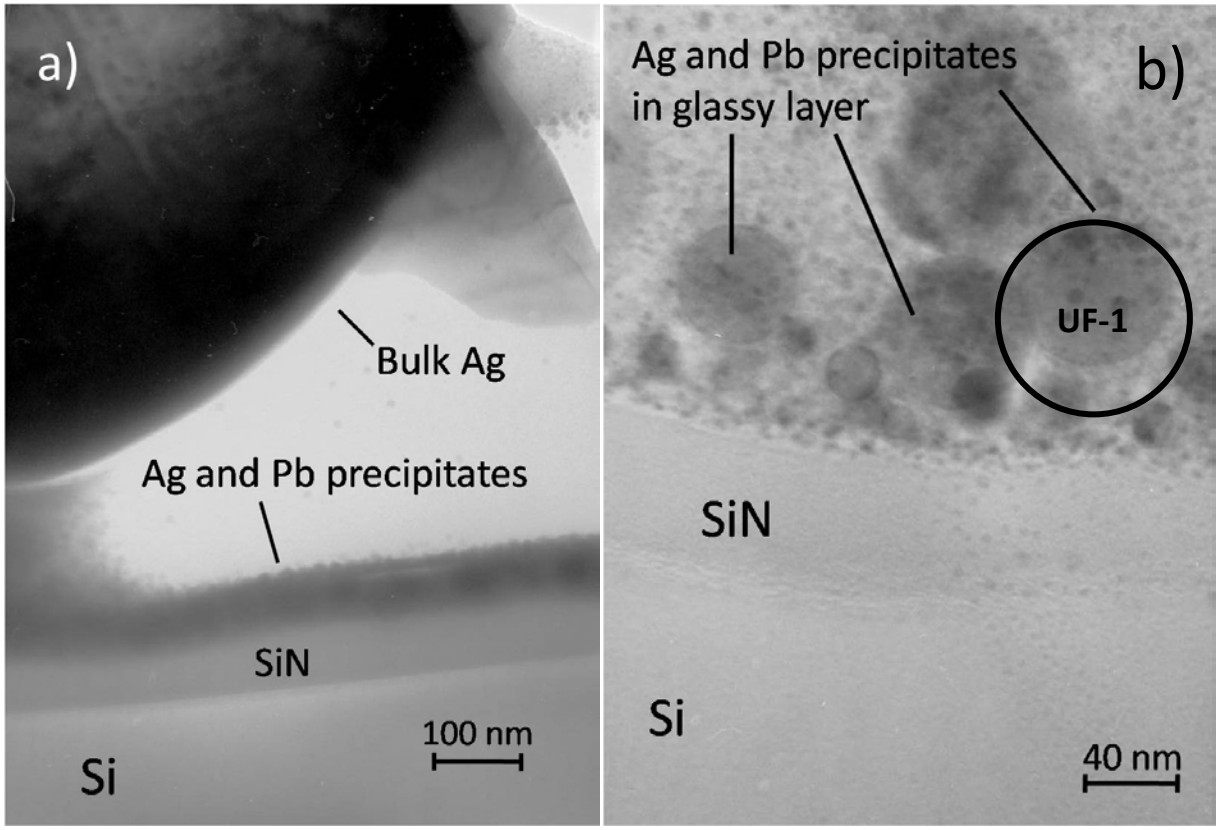

Fig. 4.9 TEM images of Ag-contact/Si-wafer interface of under fired mc-Si solar cell

In the pictures of UF cell SiN anti reflection coating can be clearly seen sitting on the top of Si wafer. In picture 4.9*a*, white area between Si and bulk Ag is a glassy layer which works as a medium for diffusion of metallic particles. Dark colored lead and silver particles can be seen precipitating in the glassy layer and on top of the SiN. A few interesting features in the first image can be distinguished:

- First, the bulk Ag has a curved surface and looks like a part of a big sphere. During firing, Ag particles do not sinter into a nice and compact structure, instead when glass frit softens and melts it flows between Ag particles, partially, due to the capillary attraction force caused by the tiny spacing between Ag particles. Pores and non-uniform surface of the bulk silver is formed. It causes different thickness of the glassy layer at the interface of the Ag bulk and the Si wafer.
- Second, many particles can be seen between bulk Ag and Si on the left side of the figure 4.9*a*, where the thickness of the glassy layer is smallest. No metallic particles precipitation in glassy layer can be seen where the thickness is larger.

In UF cells the main problem causing high series resistance is the SiN layer. It is a strong dielectric material used in electronics as an insulator. Firing temperature was probably too low to activate ARC etching mechanism so approximately 50 nm thick SiN layer makes an insulating barrier which is hard for the photoelectrons to cross. In fig. 4.9*b* some precipitates above the SiN layer were imaged. EDS analysis of area UF-1 confirmed that these were Pb and Ag particles (Fig. 4.10).

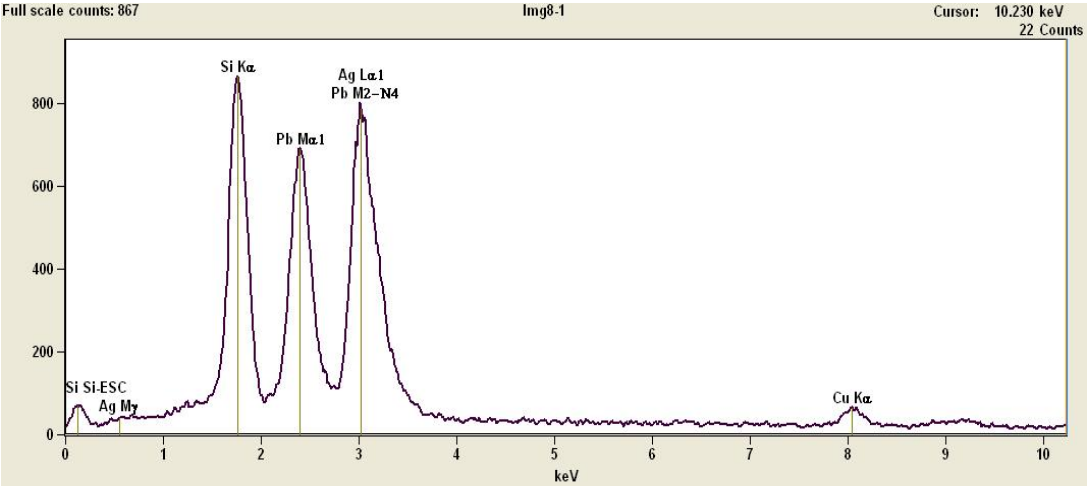

Fig. 4.10 EDS spot analysis spectrum of area UF-1 from UF cell

Images of OPF cell are shown in figure 4.11.

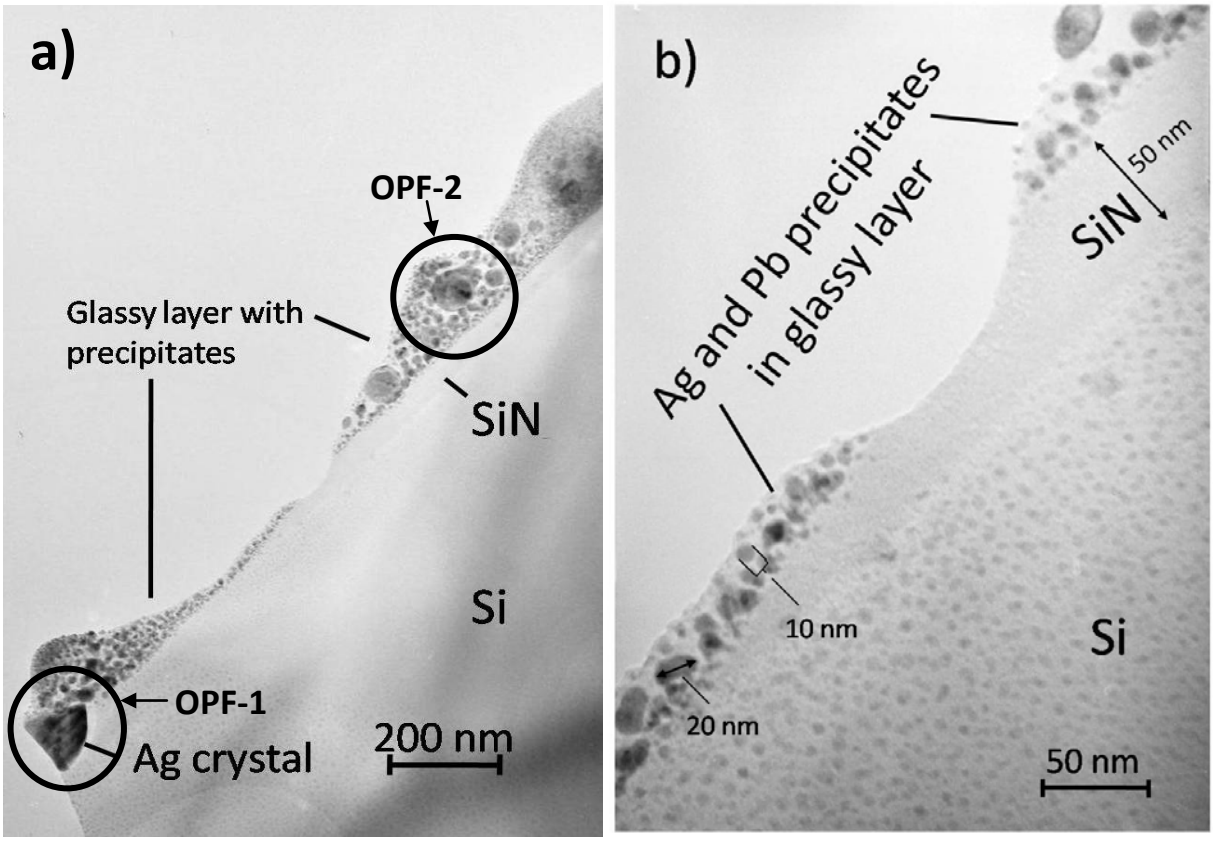

Fig. 4.11 TEM images of Ag /Si interface of optimally fired mc-Si solar cell

Image 4.11a perfectly reflects the general trend considering the Ag/Si interface of optimally fired cells. Several samples were investigated and in some of them the SiN layer could still be seen, in others it was etched away and the glassy layer, with Ag and Pb precipitates, was in contact with the Si wafer. In last group of samples some Ag crystallites grown into the Si surface were observed. In image 4.11a all three zones are in presence. On the right side of the sample the 50 nm thick SiN layer is apparent. The ARC should be about 50 nm thick before metallization which shows that in some regions the conditions for the SiN etching are unfavorable. On the left side the SiN is etched away and at the bottom left corner silver crystal grown into the Si could be seen. The crystal is about 100 nm in length and had grown 100 nm into the Si wafer. Figure 4.11b is the middle part of image 4.11a, but at higher magnification. Here a gradual change of thickness of the SiN layer is signified. The size of precipitated particles varies from <10 nm to 20 nm in diameter. Distances between the particles are mostly smaller than 3 nm. Unfortunately, most of material above Si was removed during ion milling and exact interface structure is not

clear. In image 4.11a a cluster of larger particles was observed above the silver crystal. The size of some of the particles exceeds 30 nm in diameter, while the distances between them were measured to be as long as 15 nm. EDS spectra (figure 4.12) shows the composition of zones OPF-1 and OPF-2.

The reduction of series resistance in OPF cells is caused by the areas where SiN layer is etched away. There is no insulating layer which impedes the current transport and electrons are able to move from Si wafer into the glassy layer where a large amount of Pb and Ag particles of different sizes are close apart (less than 3 nm). This distance is sufficiently small for electrons to effectively tunnel between these particles and this is expected to be the most determinant type of current collection.

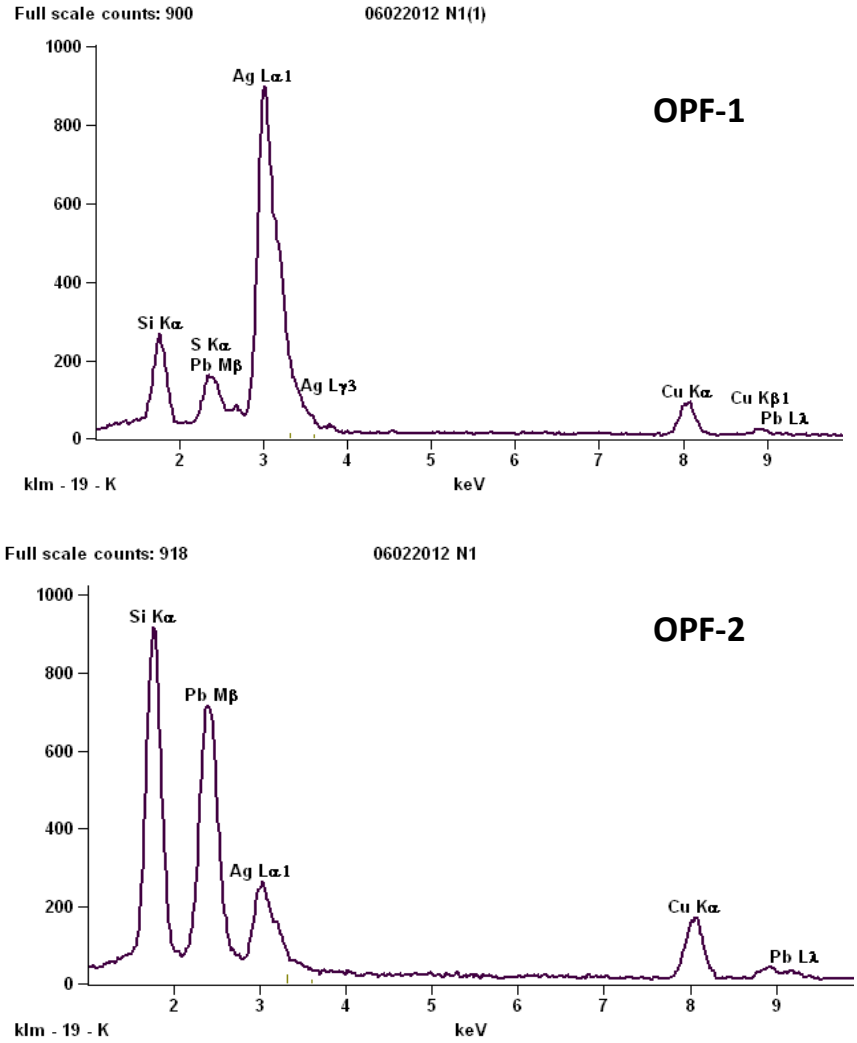

Fig. 4.12 EDS spectra of zones OPF-1 and OPF-2 from OPF solar cell

Images of OF cell are shown in figure 4.13.

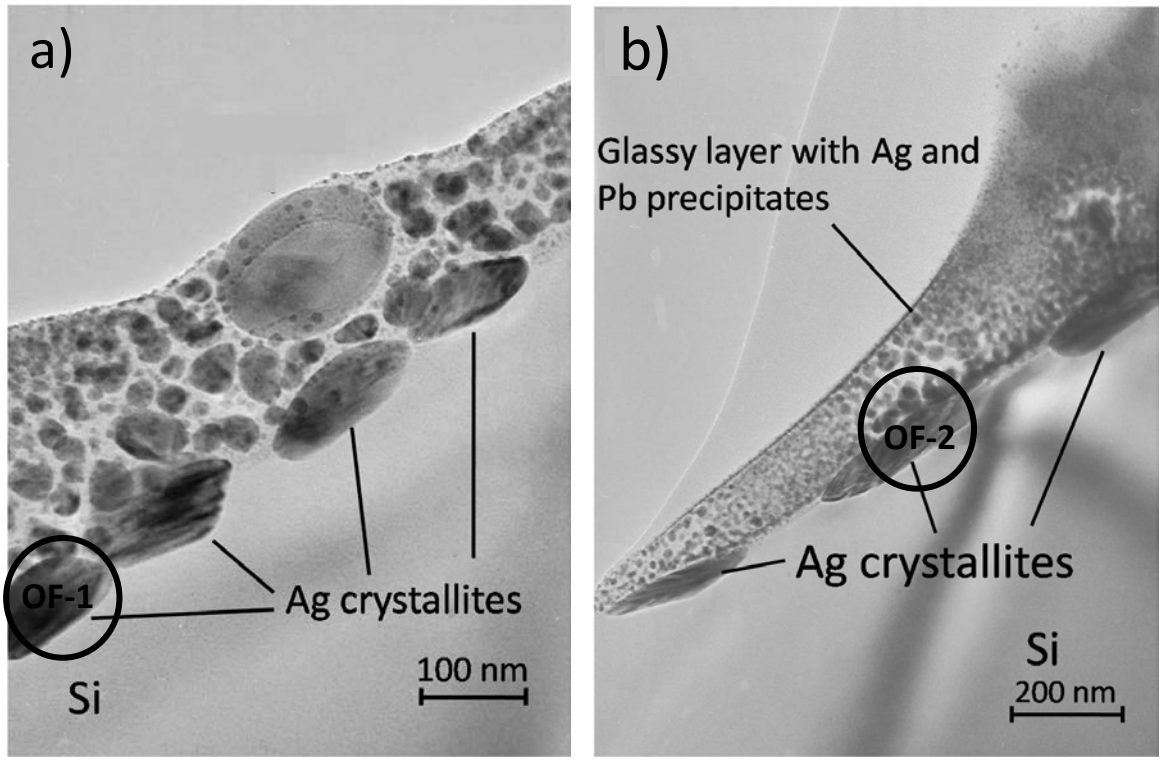

Fig. 4.13 TEM images of Ag /Si interface of over fired mc-Si solar cell

In images of OF cells no SiN layer could be observed, however, the number of silver crystallites increased dramatically. In picture 4.13b an interesting feature is observed: just above Ag crystallites there are less but bigger Pb and Ag particles. Size varies between 10 and 60 nm. Some of the large colloids are 30 nm apart which significantly reduce the tunneling probability.

It is expected that in over fired cells the firing temperature is high enough to etch away SiN layer. What is more, when Ag particles reach Si surface they tend to nucleate. As crystal starts to grow on Si surface it works as a nucleation center for other Ag precipitates and drains them. Ag crystallite grows at the expense of Ag particles precipitated in glassy layer and causes the vicinity of the crystallite to be depleted in the Ag particles. As a result, electrons which are collected by the crystallites are less likely to reach the bulk Ag contact. At the same time, Pb and Ag particles grow in larger colloids because of sintering effect which is faster at higher temperatures. Larger particles mean longer distances between them and tunneling becomes not as effective as in the optimally fired cells.

EDS spot analysis (Figure 4.14) confirms that crystallites grown on Si surface are silver.

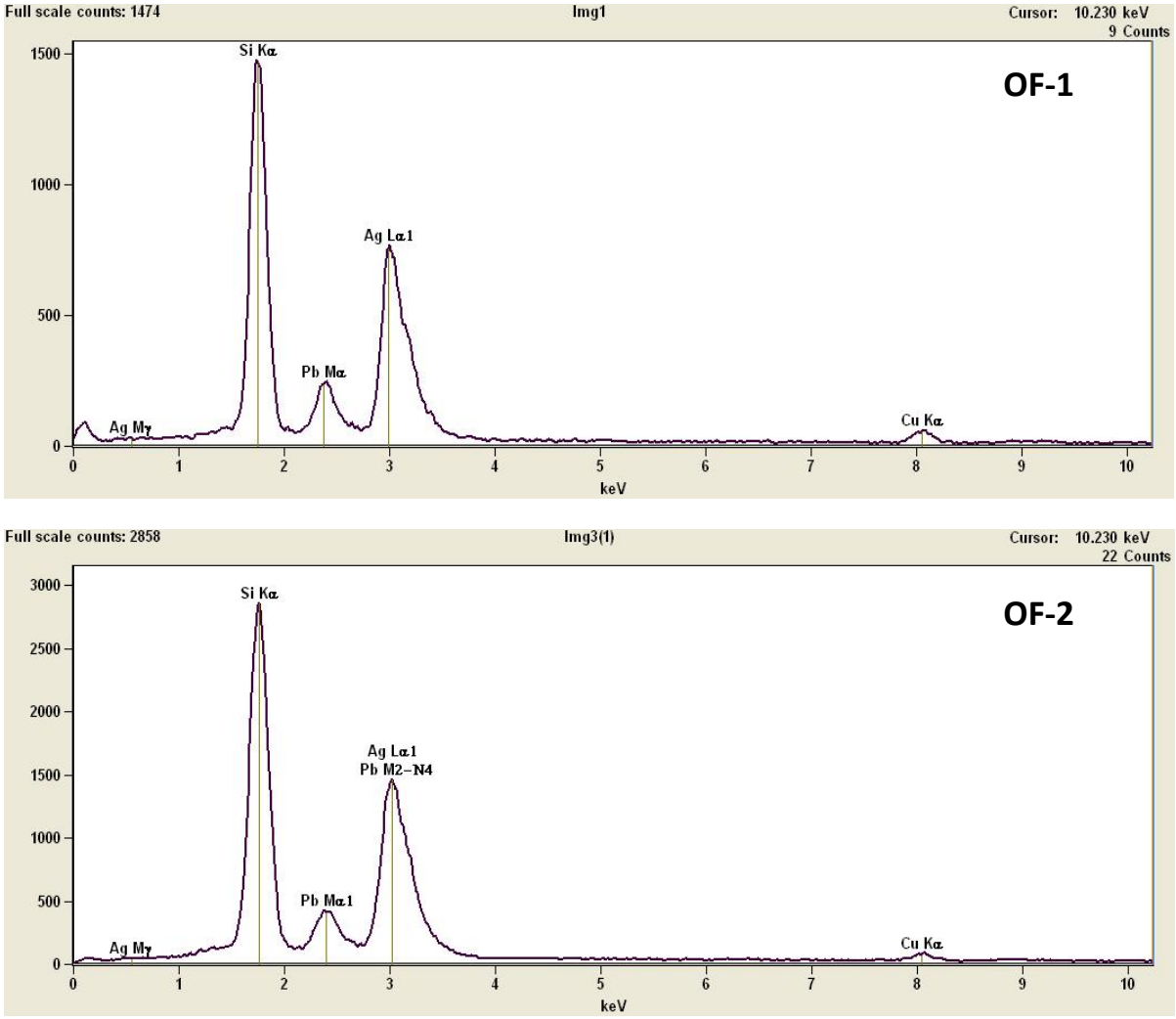

Fig. 4.14 EDS spectra of zones OF-1 and OF-2 from OF solar cell

4.4.2 Crystalline-Si cells

Images of UF cell are shown in figure 4.15.

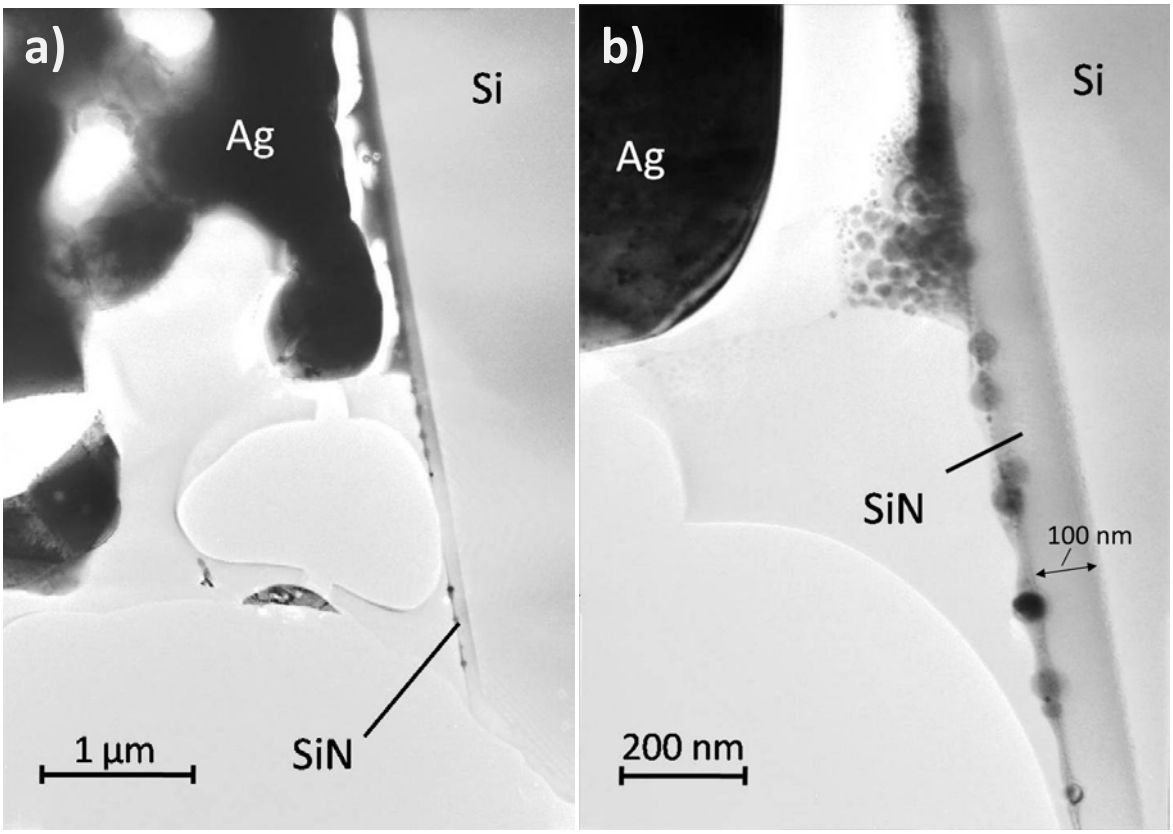

Fig. 4.15 TEM images of Ag /Si interface of under fired c-Si solar cell

In figure 4.15a the shape of Ag bulk is nicely represented. Rounded endings, porous structure and pores filled with glass tell about the intermixing of glass and Ag molten phases at high temperatures. A small gap between the Si and the bulk Ag is filled with glass as well. Traces of Ag and Pb particles towards the Si surface are still observable. However, in areas where the bulk Ag is close to the Si many more particles can be seen, while in areas where glass layer is thicker only a couple of them exist. Thick and uniform SiN layer shows that temperature is too low for the SiN etching reaction to take place. The thickness of the SiN layer is about 100 nm. Similarly to the mc-Si cells, SiN is a strongly insulating layer causing high series resistance and low efficiency.

Images of OPF cell are shown in figure 4.16.

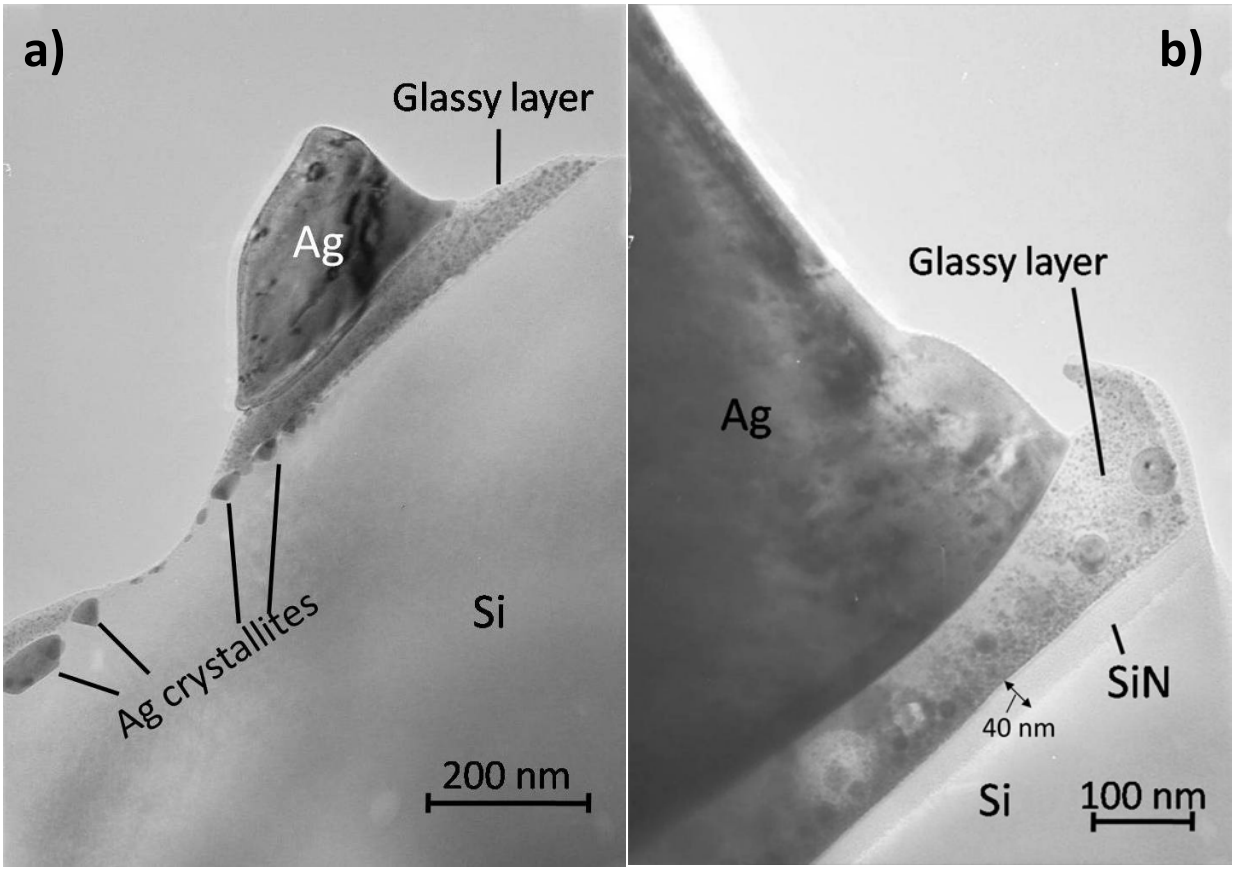

Fig. 4.16 TEM images of Ag /Si interface of optimally fired c-Si solar cell

Same as in the mc-Si, OPF cell of the c-Si cell has three types of interface structure. In figure 4.16a the SiN is completely etched away. Some crystallites are grown on the left side of the picture, while on the right side a direct connection of glassy layer and Si wafer is observed. Figure 4.16b shows that even if the distance between the bulk Ag and the Si is about the same as in picture *a* (about 100nm), the interface structure is very different. In image 4.16b the SiN is about 40 nm thick. It shows that etching was in process but was not complete. Both pictures are taken from the same sample and these two areas can be several micrometers apart, so there cannot be any major firing temperature differences. It looks like two main parameters, firing temperature and distance between the bulk Ag and the Si, are the same but the structure of the interfaces has a deciding difference. This means that there are other factors determining the structure of Ag/glassy-layer/Si interface. It also emphasizes the difficulty of explaining contact formation mechanism on microscopic scale.

The effectiveness of these cells could again be explained by current transport through tunneling mechanism through glassy layer which is abundant in metallic nano-particles.

Images of OF cell are shown in figure 4.17.

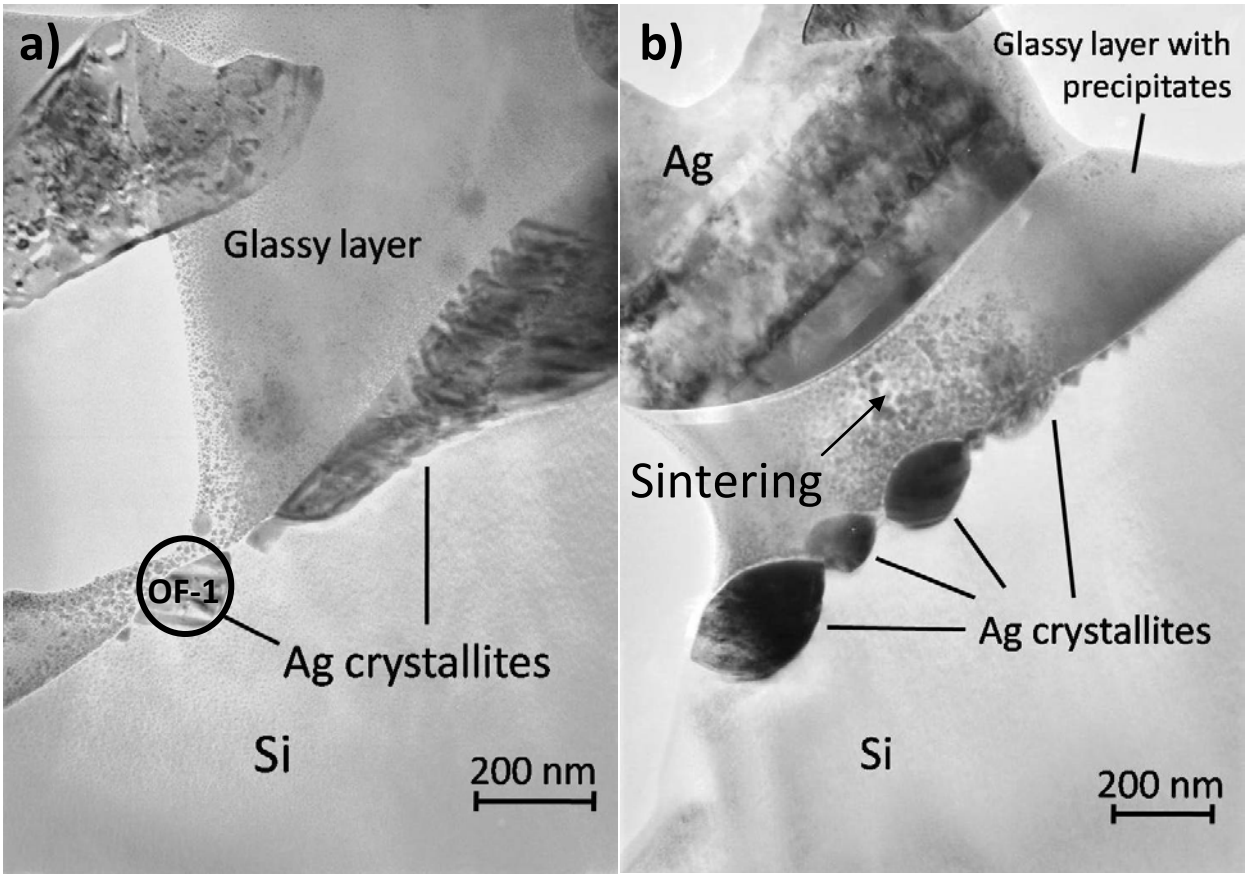

Fig. 4.17 TEM images of Ag /Si interface of over fired c-Si solar cell

The monocrystalline over fired cell has the same features as the multicrystalline cell. A lot of crystallites are apparent and no SiN above the Si wafer was detected. In figures 4.17 it can be seen that crystallites are much larger in size than in mc-Si cells. They grew 100-200 nm into the Si surface while a huge crystal in figure 4.17a (right side) has penetrated Si wafer about 300 nm and might cause cell shunting.

Crystallite growth in expense of small Ag particles is observable in figure 4.17b. In the mean time, smaller particles sinter into larger colloids and cause less conductive glassy layer. In general, OF c-Si cell distinguished with a Si surface nicely decorated with Ag crystallites along large area of the sample (figure 4.18).

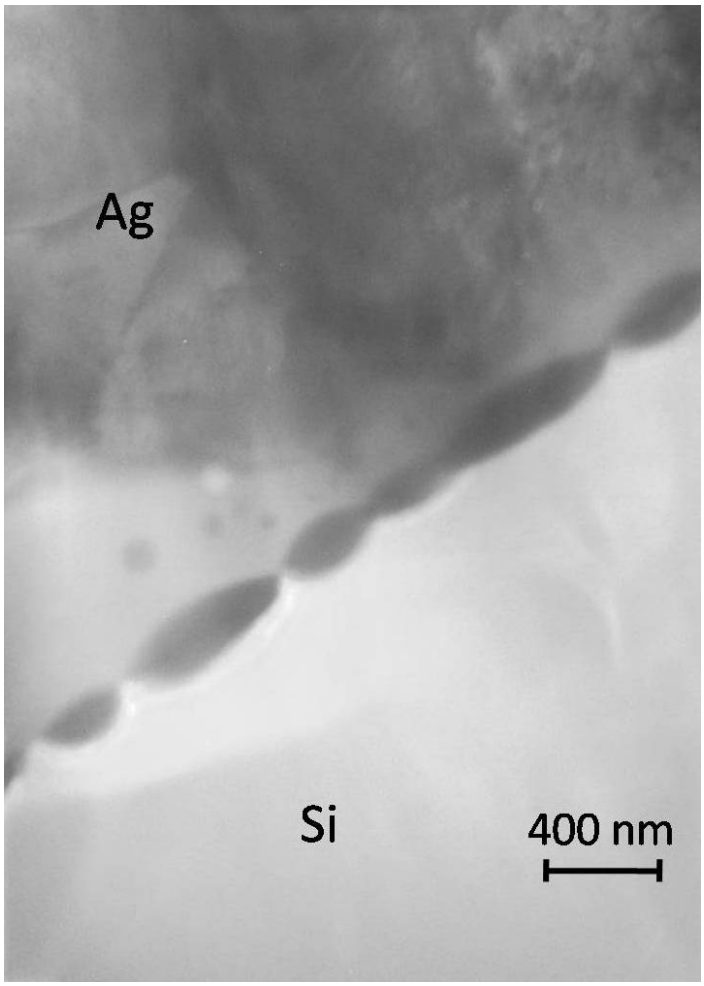

Fig. 4.18 TEM image of Ag /Si interface with many Ag crystallites grown on the Si surface

Finally, we conclude that the Ag crystallites are not necessary for effective current transport. The most effective mechanism for current collection is the tunneling of the photoelectrons through Pb and Ag precipitates. These conclusions are consistent with Z. G. Li findings in [2.20]. The direct connections between the Ag crystallites grown into the Si wafer and the bulk Ag have not been observed. To authors knowledge no such connections were confirmed in any other articles. As concluded by K. K. Hong in [2.16, 2.19] during etching of the SiN layer there will always be some amount of glass produced. This means that everywhere, where the SiN is etched away there will be a glassy layer and no direct connections of the bulk Ag and the Si wafer are possible.

4.5 Diffraction

Diffraction pattern analysis was performed in order to determine the orientation of silver crystallites grown on the silicon surface. Diffraction pattern was taken from zone OF-1 of the over fired c-Si cell. The smallest aperture was not small enough to cover only the silver crystal so reflections of silicon can be seen as well. The two patterns of silver and silicon are shown in a combined pattern in figure 4.19a, together with untangled patterns in 4.19b and c.

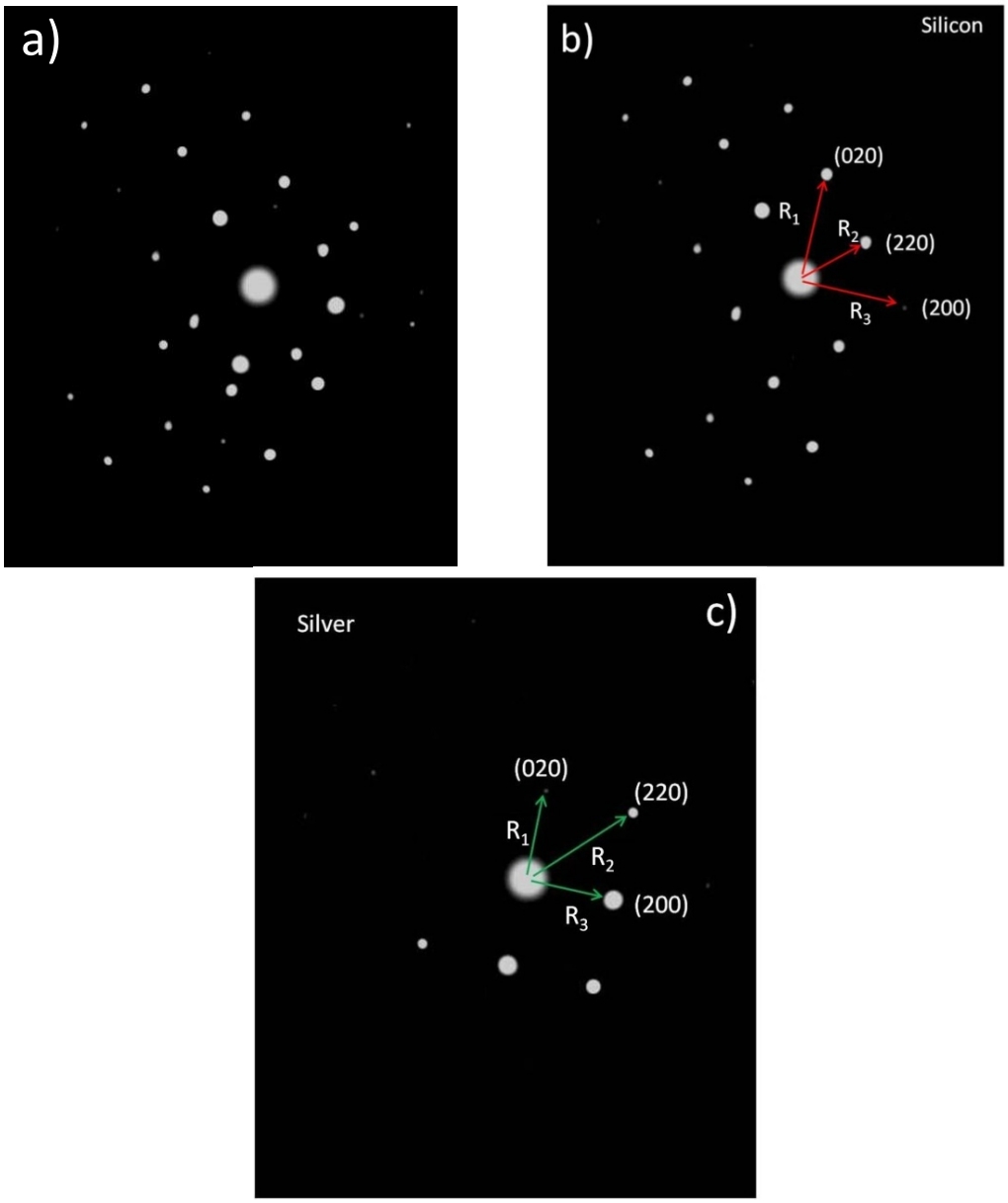

Fig. 4.19 Diffraction patterns of a) silver and silicon combined together; b) just Si DP untangled from pattern *a*; c) just Ag DP untangled from pattern *a*.

Reference images of Si and Ag were used to untangle the patterns. Reflections of silicon were determined by calculating *d* values from distances R_1, R_2, R_3. According to calculations patterns were indexed as shown in figures 4.19 *b* and *c*. Finally, the diffraction pattern with combined patterns of Si and Ag was indexed and is sketched in figure 4.20.

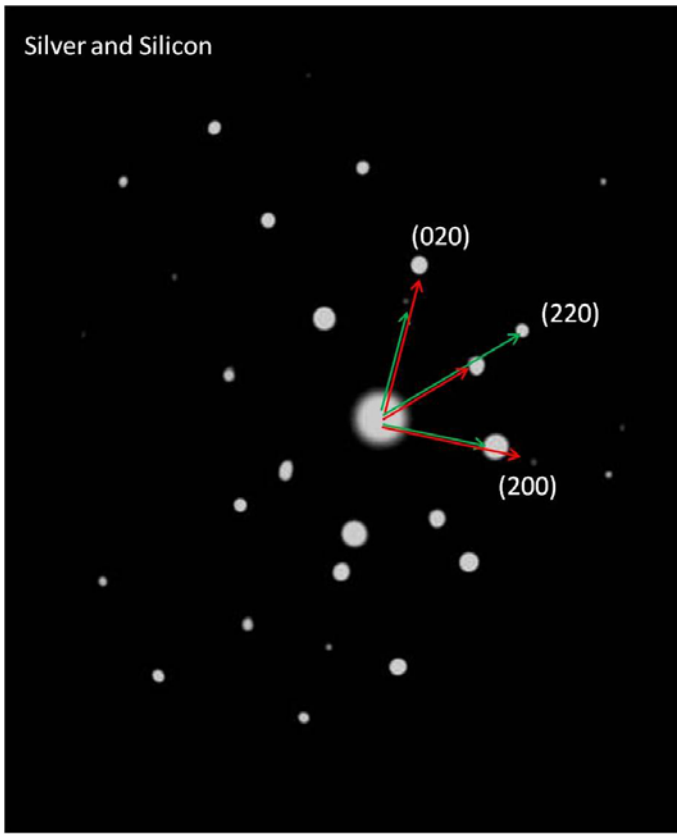

Fig. 4.20 Indexed diffraction pattern of silver crystallite grown on silicon surface

This pattern clearly shows that orientations of the silicon wafer and the silver crystallite match perfectly. However, the Ag crystallite is not sitting on a flat surface of Si; instead, it is grown as a triangle into Si surface. This means that Ag crystallite is a pyramid shaped and is touching silicon at different surface.

5. Conclusion

Multicrystalline and monocrystalline cells were fired at varying peak temperatures and optimization was achieved at 900˚C for mc-Si and 960˚C for c-Si cells.

Using solar simulator and series resistance mapping it was determined that lower performance of the under fired cells was caused by series resistance while in the over fired cells both parasitic resistances had influence on the FF reduction.

TEM investigation confirmed different structures of contact/Si-wafer interface for under fired, optimally fired and over fired cells.

In the under fired cells the SiN insulating layer was observed. This layer was the main factor limiting effective current transport from the wafer to the bulk silver.

In the optimally fired cells three types of Ag/Si interface structures were found. In some areas SiN was still apparent, in others it was completely etched away and Si wafer was in direct contact with glassy layer with a lot of Ag and Pb precipitates. Particles in glassy layer were in a tunneling range between each other (<3 nm) and were expected to make a path for electrons to travel between the bulk Ag and the Si wafer. In another regions Ag crystallites grown into Si surface were detected.

Over fired cells possessed Si surface nicely decorated with Ag crystallites. The crystallites grew in expense of Ag precipitates which tended to nucleate at Si surface and then drained Ag particles from the vicinity. At higher temperatures sintering effect caused precipitates to accumulate into larger colloids. Both these effects caused larger distances between Ag and Pb particles and between Ag crystallites. Therefore, tunneling was less likely to happen and Ag/glassy-layer/Si interface became less conductive.

We suggest that the most determinant current transport mechanism is electron tunneling between the Si wafer and the Ag bulk through Ag and Pb nanoparticles. No direct Ag bulk and Si wafer connections were witnessed during this project.

6. Further work

In this work multicrystalline cells were investigated and monocrystalline CZ cells oriented along (100) axis were used to supplement the data collected from multicrystalline cells. However, due to the lack of time only cells of this orientation were checked, while cells of different orientations (010) and (111) would be very interesting to look at.

Only one type of paste was used for front contacts. Paste properties are very crucial for metallization process. Paste parameters like composition or viscosity could determine the physics and chemistry of contact formation so it would be an interesting field for future work as well.

Variation of cooling rate is expected to have influence on crystal size during crystallization. A structural Si/Ag interface investigation of cells cooled at different rates would be an interesting topic.

Nano-scale series resistance mapping could lead to a better understanding of how electrons are collected at different parts of contact finger and would let to more accurately choose material for TEM investigation.

7. References

[1.1] U.S. Energy information administration, *International energy outlook 2011*, 2011

[1.2] Solomon, S., D. Qin, M. Manning, Z. Chen, and H.L. Miller, *Contribution of Working Group I to the Fourth Assessment Report of the Intergovernmental Panel on Climate Change*, 2007

[1.3] BP solar, *Statistical Review of World Energy 2009*, 2009

[1.4] M. Stohr, R. Bischof, H. Dufner, and J. Gregory, *Conference Proceedings, 13th EC PVSEC*, **1183-1185**, 1995

[1.5] M. Osborne, "*IMS Research raises global PV installation forecast for 2011*", article in www.pv-tech.org, 2011

[2.1] Jenny Nelson, "*The Physics of Solar cells*", Imperial college, UK, 2002

[2.2] A. Luque and S. Hegedus, "*Handbook of Photovoltaic Science and Engineering*", Wiley, 2003

[2.3] S.Vengris, "*Solid state electronics*", Vilnius, 2008 (Lithuanian)

[2.4] C. B. Honsberg and S. Bowden, *PVCDROM online application (*http://pveducation.org/)

[2.5] N. B. Mason and D. Jordan, *Proceedings for 10th E.C. Photovoltaic Solar Energy Conference*, Lisbon, pp. **280-283**, 1991

[2.6] S. R. Wenham and M. A. Green, "*Buried Contact Solar Cell*", 1988

[2.7] D. L. Meier and D. K. Schroder, *IEEE Transactions on Electron Devices 31*, **647-653**, 1984

[2.8] M. A. Green, K. Emery, Y. Hishikawa, and W. Warta, *Progress in Photovoltaics: Research and Applications, 2011*

[2.9] J. Zhao, A. Wang, and M. A. Green, *Solar Energy Materials and Solar Cells* 66, **27-36**, 2001

[2.10] O. Schultz and S.W. Glunz, *19th EU PVSEC*, 2004

[2.11] J. F. Nijs, J. Sclufcik, J. Poortmans, S. Sivoththaman, and R. P. Mertens, *IEEE Transactions on Electron Devices 46,* **1948-1969**, 1999

[2.12] J. G. Fossum, *IEEE Transactions on Electron Devices, vol. 24, no. 4,* **322 - 325**, 04/1977

[2.13] S. Kontermann, M. Horteis, M. Kasemann, A. Grohe, R. Preu, E. Pink, and T. Trupke, *Solar Energy Materials & Solar Cells 93,* **1630-1635**, 2009

[2.14] J.Y. Huh, K.K. Hong, S.B. Cho, S.K. Park, and B.C. Lee, *Materials Chemistry and Physic*, 2011

[2.15] M. M. Hilali, S. Sridharan, C. Khadilkar, A. Shaikh, A. Rohatgi, and S. Kim, *Electronic Materials,* **Vol. 35, No. 11,** 2006

[2.16] K. K. Hong, S. B. Cho, J. Y. Huh, H. J. Park, and J. W. Jeong, *Metals and Materials International,* **Vol. 15, No. 2,** 2009

[2.17] K. T. Butler, P. E. Vullum, A. M. Muggerud, E. Cabrera, and J. H. Harding, *Physical Review B83,* **235307,** 2011

[2.18] C. Ballif, D. M. Huljic, G. Willeke, and A. Hessler-Wyser, *Applied Physics Letters,* **82,** 2003

[2.19] K. K. Hong, S. B. Cho, J. S. You, J. W. Jeong, S. M. Bea, and J. Y. Huh, *Solar Energy Materials & Solar Cells 93,* **898**, 2009

[2.20] Z. G. Li, L. Liang, and L. K. Cheng, *Journal of Applied Physics,* **105, 066102,** 2009

[2.21] C. H. Lin, S.P. Hsu, and W. C. Hsu, *"Silicon solar cells: structural properties of Ag-Contacts/Si-Substrate"*, ITRI, Taiwan, 2011

[2.22] R.J.S. Young and A.F. Carroll, *Proceedings of the 16th EC PVSEC,* Glasgow, **1731**, 2000

[2.23] G.C. Cheek, R.P. Mertens, R. van Overstraeten, and L. Frisson, *"Thick-film metallization for solar-cell applications", IEEE Transactions On Electron Devices, vol. 31*, **602**, 1984

[2.24] M. Prudenziati, L. Moror, B. Morten, and F. Sirotti, *Active and Passive Electronic Compounds 13,* 1989

[2.25] T. Nakajima, A. Kawakami, and A. Tada, *International journal for Hybrid Microelectronics*, 1983

[2.26] M. M. Hilali, B. To, and A. Rohatgi, *Proc. 14th Workshop on Crystalline Silicon Solar Cell & Modules: Materials and Processes*, 2004

[2.27] D. B. Williams and C.B. Carter, "*Transmission Electron Microscopy: A Textbook for Materials Science"*, Springer Science & Business Media, 2009

[2.28] A. Olsen, "*The theory and practice of analytical electron microscopy in materials science"*, **Vol I, Vol II**, 2008

[3.1] H. Kampwerth, T. Trupke, J. W. Weber, and Y. Augarten, *Applied Physics Letters 93*, **202102**, 2008

[3.2] T. Trupke, R. A. Bardos, M. D. Abbott, and J. E. Cotter, *Applied Physics Letters 87*, **093503**, 2005

[3.3] T. Fuyuki, H. Kondo, T. Yamazaki, Y. Takahashi, and Y. Uraoka, *Applied Physics Letters 86*, **262108**, 2005

[3.4] T. Trupke, E. Pink, R.A. Bardos, and M.D. Abbott, *Applied Physics Letters 90*, **093506**, 2007

[3.5] D. B. Williams and C.B. Carter, "*Transmission Electron Microscopy: A Textbook for Materials Science"*, Springer Science & Business Media, 2009

[4.1] http://www.ferro.com/non-cms/ems/Solar_2010/leadfree/53-140-Series.pdf

[4.2] http://www.ferro.com/non-cms/ems/Solar_2010/frontsurfacemetallizations/NS-33-512.pdf